Ocean Wave Dynamics and El Niño

EDWIN K. SCHNEIDER, BOHUA HUANG, AND J. SHUKLA

Center for Ocean–Land–Atmosphere Studies, Calverton, Maryland

(Manuscript received 3 March 1994, in final form 31 March 1995)

ABSTRACT

The response of an ocean general circulation model to specified wind stress is used to understand the role of ocean wave propagation in the evolution of El Niño events in sea surface temperature (SST) in the equatorial Pacific Ocean. In a control experiment the ocean model reproduces observed equatorial Pacific interannual variability in response to forcing by the observed wind stress. The ocean model is then forced with the same wind stress but with the time evolution of the wind stress forcing reversed. An analysis of the anomalies from the annual cycle in these two experiments delineates the parts of the response that are in equilibrium with and out of equilibrium with the wind stress forcing.

In the western equatorial Pacific the SST anomalies are in equilibrium with the wind stress anomalies. In the eastern equatorial Pacific the SST anomalies are not in equilibrium with the wind stress anomalies but rather tend toward equilibrium with the upper-ocean heat content anomalies.

The experiment demonstrates that the heat content is not in equilibrium with the wind stress forcing either on or near the equator. Very close to the equator the slope of the thermocline is in equilibrium with the wind stress, but the mean heat content is far from equilibrium. Slightly off of the equator in the western Pacific westward propagating heat content anomalies appear to originate in regions of strong wind stress forcing and then propagate to the western boundary. These westward propagating anomalies also depart significantly from equilibrium with the wind stress forcing.

Additional experiments allow these westward propagating anomalies to be identified as freely propagating Rossby waves. The Rossby waves are shown to determine the equatorial heat content response to the wind stress forcing when they arrive at the western boundary and to be responsible for the nonequilibrium behavior of the equatorial mean heat content.

A simplified coupled model is derived by fitting the results and estimating parameter values from the numerical experiments. In this model the time delay introduced by the Rossby waves is responsible for coupled instability, and dependence of the Rossby wave amplitude on the frequency of the forcing is responsible for the long period of the coupled oscillations.

1. Introduction

The importance of coupled oscillations of the tropical Pacific Ocean and the tropical atmosphere on interannual timescales (the El Niño–Southern Oscillation phenomenon or ENSO) has been recognized for some time (Bjerknes 1966, 1969). These coupled oscillations consist of alternating warm sea surface temperature–enhanced rainfall and cold sea surface temperature–decreased rainfall periods in the central and eastern equatorial Pacific. Simulations of both ENSO and the tropical Pacific annual cycle with coupled atmosphere–ocean general circulation models are improving rapidly, but significant deficiencies remain. Neelin et al. (1992b) summarizes the state of the art at that point in time. More recent results are given by Latif et al. (1993) and Robertson et al. (1994).

Corresponding author address: Dr. Edwin K. Schneider, Center for Ocean–Land–Atmosphere Studies, 2041 Powder Mill Road, Suite 302, Calverton, MD 20705.
E-mail: schneide@cola.iges.org

Bjerknes (1969) proposed an unstable air–sea interaction mechanism by which sea surface temperature (SST) anomalies from the annual cycle could amplify due to coupling with the atmosphere. The mechanism is that a reduction in the easterlies in the equatorial Pacific, which maintain a relatively warm western Pacific and cold eastern Pacific, would lead to a warmer central and eastern Pacific, which would further reduce the easterlies, eventually leading to a warm, El Niño, event. A reversal of the argument explains the onset of a cold, La Niña, event. The structure and evolution of unstable air–sea interactions is discussed by Philander et al. (1984) and Philander (1985). However, the Bjerknes mechanism does not explain the demise and alternation of the warm and cold events.

A central problem in understanding the observed system is to explain the relatively long period of the coupled oscillations, which is on the order of three to five years. It is evident that such a long timescale must arise from some aspect of ocean dynamics; the atmosphere can be considered to be in equilibrium with the ocean on these timescales.

Wyrtki (1985) identified a cyclic behavior of anomalies of the tropical Pacific sea level (equivalently the depth of the 20°C isotherm, also referred to as "thermocline depth" or "thermocline displacement" in the following and used interchangeably with "heat content") associated with El Niño. He attributed the timescale of the El Niño cycle to the discharge of stored warm water in the equatorial Pacific thermocline during warm events, associated with Kelvin wave reflection from the eastern boundary, and the slow deepening of the thermocline and recharging of this warm water reservoir in between the warm events. In Wyrtki's picture, the heat content anomalies in the thermocline influence the SST and provide the memory for the oscillations.

Cane and Zebiak (1987) describe results from a coupled model and follow Wyrtki (1985) in attributing an important role to the subsurface heat storage for producing El Niño. Cane and Zebiak (1987) pointed out that in their model the zonal mean heat content leads the wind forcing and suggested that the meridional transfer of warm subsurface water between equatorial and higher latitudes is responsible for the transition between warm and cold events. The meridional mass exchange was explained as due to the mismatch in time and space scales of equatorial Kelvin and Rossby waves, both of which are forced by the wind stress anomalies.

Cane and Zebiak (1987) also noted that at the low frequencies characteristic of ENSO the pressure gradient due to the longitudinal slope of equatorial heat content anomalies balances the wind stress forcing (Philander 1979, 1981; Cane and Sarachik 1981; Cane 1992; Neelin et al. 1994). McPhaden and Taft (1988) verified this equilibrium relationship from observations. This equilibrium relationship applies to the slope but not necessarily the zonal mean of the heat content anomalies. This is an important result that will be useful later in the paper.

Schopf and Suarez (1988), Suarez and Schopf (1988), and, independently, Battisti and Hirst (1989) suggested the "delayed oscillator" mechanism to explain the oscillatory nature and multiyear timescale of ENSO. The delayed oscillator relies on two properties of the near-equatorial upper ocean. One is that information propagates rapidly eastward in the form of Kelvin waves and more slowly westward in the form of Rossby waves. The other is that the thermocline is significantly deeper in the western Pacific than in the eastern Pacific; consequently, SSTs are much more sensitive to thermocline displacements in the eastern than in the western Pacific. The explanation given by Schopf and Suarez (1988) is that an isolated equatorial westerly wind stress anomaly will lead to a disturbance in which air–sea coupling is important (that is, with a significant SST signal) propagating toward the east as a deepening of the thermocline. The coupling leads to growth of a warm episode by an unstable air–sea interaction. Also, uncoupled (insignificant SST signal) Rossby waves propagate slowly (phase speed one-third that of the Kelvin wave) westward from the disturbed region, reflect off of the western boundary of the ocean basin, and then propagate rapidly to the east as a shallowing of the thermocline, catching up to and cancelling the coupled disturbance and leading to the demise of the warm episode. The oscillation then proceeds with reversed sign of the wind stress, SST, and thermocline depth anomalies. The period of the oscillation is longer than twice the sum of the travel time of the information to the western boundary and then back to the disturbed region. The delayed oscillator mechanism requires the SST to respond sensitively to the subsurface heat content anomalies in the eastern Pacific.

Battisti and Hirst (1989) derived a simple analog model for the delayed oscillator mechanism from the time-dependent SST equation. They were able to describe the dependence of the oscillations in this model on parameters such as basic state, local coupling strength, and assumed delay time. The delay time was specified and represented the effects of ocean dynamics associated with the phase speed of freely propagating waves, as well as geometrical factors such as basin size and location of the forcing. They found that a wide range of periods for unstable oscillations, ranging from the order of 1 year to infinity, could be obtained for the same delay time by varying other parameters. This sensitivity resulted from a competition between the local Bjerknes instability mechanism and the delayed effects of reflections from the western boundary. Although the delay time of freely propagating waves is necessary for oscillatory behavior, the individual freely propagating waves would not be identifiable as the period becomes long.

Schopf and Suarez (1990) and Cane et al. (1990) were able to derive time delay systems for coupled atmosphere–ocean behavior using models that included explicit solution of the linear time-dependent shallow water equations for the evolution of the thermocline displacement anomalies. The wind stress anomalies were taken to be proportional to the thermocline displacement anomalies in the eastern Pacific, effectively assuming equilibrium between eastern Pacific SST and thermocline displacement anomalies and no influence of SST anomalies elsewhere on the wind stress anomalies. The idealized coupling allowed analytic or quasi-analytic solutions to be found. Time dependence and hence the potential for unstable oscillatory behavior arose from ocean wave dynamics in the Schopf and Suarez (1990) and Cane et al. (1990) models.

Chao and Philander (1993) examined the response of an oceanic general circulation model (OGCM) of the Pacific to the wind stress forcing observed from 1967 through 1978. They noted that they could not identify the individual freely propagating equatorial waves and reflections that were seen in the Schopf and Suarez (1988) results. Chao and Philander (1993) described a systematic eastward propagation of equatorial

heat content anomalies near the equator with a phase speed much smaller than that which would be expected of equatorial Kelvin waves. The observed equatorial wind stress anomalies also appear to propagate slowly eastward in the western and central Pacific. At 9°N and 8°S westward propagation of heat content anomalies was noted to the west of the date line. They explained the slow phase speeds at the equator as due to the superposition of many different waves forced at different times and places, which is basically the same interpretation as the modified delayed oscillator mechanism of Battisti and Hirst (1989), Schopf and Suarez (1990), and Cane et al. (1990). The westward propagation off the equator in the western Pacific was attributed to an equilibrium response to the local winds, but no estimate of the phase speed was given in this region for comparison to Rossby wave phase speeds.

Neelin (1991), Neelin et al. (1992a), and Hao et al. (1993) showed that coupled air–sea oscillations could occur even in the limit when delay times were eliminated from equations governing the thermocline displacement. This case was called the "fast wave limit" (Neelin 1991). If the SST provided memory to the system by heat storage in the mixed layer ("slow SST") in the fast wave limit, unstable coupled oscillations could occur. The fast wave limit was obtained formally from the linear shallow water equations forced by wind stress by neglecting time derivatives [e.g., Hao et al. 1993, their Eq. (2.12)]. Consequently, in the fast wave limit the thermocline displacement anomalies throughout the basin are in equilibrium in a global sense with the wind stress anomalies. The thermocline displacement at any point responds instantaneously with zero time lag to a wind stress change at any other point. Neelin et al. (1992a) noted that in the fast wave limit a deep thermocline in the west can precede each warm event, and slow eastward (or even westward) propagation of equatorial heat content anomalies can occur. Therefore, the phase relations found in the heat content in observations or models do not by themselves prove the importance of wave delay times to the occurrence of the coupled oscillation.

The physics of the fast wave–slow SST limit and the converse, the slow wave–fast SST limit in which thermocline displacements are not in equilibrium with wind stress but SST is in equilibrium with thermocline displacements (Schopf and Suarez 1990; Cane et al. 1990), seem to be very different. In the fast wave–slow SST limit the thermocline displacements are in equilibrium with the wind stress and the surface layer provides the memory for the system, while in the slow wave–fast SST limit the surface layer is in equilibrium with the subsurface heat content and the heat content provides the memory. However, Jin and Neelin (1993a,b) and Neelin and Jin (1993) demonstrated that these regimes are related at least in a formal sense. A wide range of behaviors can be produced in various limiting and intermediate regimes and many appear to be realistic. It would be desirable for practical reasons to find tests to isolate the important properties of the realistic regime.

The position on the fast wave–slow wave axis of the response of an uncoupled ocean model to specified wind stress forcing can in principle be identified a posteriori by finding the dominant balances in the equations of motion as was attempted by Lau et al. (1992) in a coupled setting. The regime will depend on the imposed timescales in the wind stress forcing as well as properties of the oceanic mean state and physical parameterizations.

In this paper we describe a simple test that allows departures of the SST and heat content from equilibrium to be explicitly determined in realistic simulations of the equatorial Pacific Ocean by using realistic models and wind stress forcing. This test is applied to determine whether or not the model heat content is in equilibrium with the forcing (fast wave limit). Similarly we use the test to determine to what extent the SST is in equilibrium with the heat content (fast SST limit) or responding with a significant time lag (slow SST). The test consists of two integrations of an OGCM with specified wind stress forcing. First, a control integration is carried out in which the ocean model is forced by observed wind stresses for an extended period. Another integration is carried out in which the wind stress forcing is the same as in the control integration but applied backward in time (n.b.: this procedure is not equivalent to integrating the equations of motion backward in time). We will use the same OGCM as used by Chao and Philander (1993), except at a lower resolution, and use wind stress observations from a later period. Our control experiment is similar to the integration described by Chao and Philander (1993).

The time evolution of equatorial SST from the two integrations is compared, with the time axis for the backward-forcing case reversed relative to the control case. Then results from both cases have the same wind stress forcing at equivalent positions on the display time axis. The time axis that the results are plotted against is called the "forcing time." If the ocean model is in equilibrium with the wind stress forcing, the results from two experiments plotted in forcing time will be the same. If the ocean model is not in equilibrium with the wind stress forcing, then the results from the two experiments in this representation will differ.

If the response is in the fast wave regime, then the heat content will be in equilibrium with the wind stress and therefore will be similar in both experiments. The heat contents will of course differ in the two experiments in the delayed oscillator regime. In the delayed oscillator, slow wave regime the heat content response at time t can be thought of as due in part to the influence of the local wind stress forcing at t and in part due to the influence of remote wind stress forcing at a previous time, $t - \tau$, where the lag, τ, is determined by the wave-propagation characteristics of the ocean and the loca-

tion of the forcing region relative to the location where the response is measured. In the backward-forcing case, the response at forcing time t (i.e., at a time with the same forcing as the control case at t) will be due to the influence of the local forcing at t plus the influence of the remote forcing at $t + \tau$. For the heat content simulated by the control and backward cases to be the same, the control case would have to know the future forcing, which violates causality (except for periodic forcing).

In the subsequent sections we describe the implementation of this forward–backward experiment and examine the characteristics of the interannual variability. The results show that the tropical Pacific heat content is far from equilibrium with the wind stress forcing. Time lags due to heat storage in the mixed layer appear to be unimportant for the SST.

Results from additional distorted forcing experiments, carried out to further examine the departure from the fast wave limit, are then described. These calculate the response of the OGCM when the time evolution of the wind stress is sped up and slowed down. A simple time-delay relationship is developed empirically from the results to describe the ocean model heat content response to the observed wind stress. Implications of this empirical relationship in the fast SST limit are examined. The relationship of the results found here to the conceptual models for understanding El Niño are summarized in the concluding section.

2. Experimental design

The basic experiment consists of two integrations of a model of the tropical Pacific Ocean forced by specified wind stresses. Wind stress was obtained from observations and heat flux was parameterized as a damping to a time-independent air temperature. Huang et al. (1994) used similar techniques in their calculations.

a. The ocean model

The ocean model used in these integrations was adapted from the GFDL Modular Ocean Model (Bryan and Lewis 1979). This model is a finite-difference treatment of the primitive equations of motion on the sphere. Nonlinear vertical mixing of heat, salinity, and momentum (Pacanowski and Philander 1981) and constant coefficient horizontal mixing of heat and momentum are chosen.

The model uses moderate resolution and a limited, simplified domain. The horizontal structure of the model was chosen following Neelin (1990). The latitudinal domain is limited by rigid walls to be from 30°S to 50°N. The ocean is also limited to lie between 130°E and 80°W. Inside of that domain realistic basin boundaries are used, but there are no islands in the interior. Zonal resolution is chosen to be 3° longitude. The meridional resolution is taken to be 1° latitude between 10°S and 10°N, increasing to 4° latitude at 30°S and 30°N and 4° latitude poleward of 30°N. The horizontal diffusion coefficient is taken to be 4×10^7 $cm^2\ s^{-1}$.

The model ocean has a uniform depth of 4000 m, resolved by 13 layers. The layers depths are chosen to be approximately those used by Barnett et al. (1993). The top four layers are each 20.0 m thick, and the fifth through thirteenth layer thicknesses are 20.11, 20.92, 25.47, 45.49, 113.64, 291.45, 641.16, 1141.99, and 1619.78 m.

The results from these experiments can be considered to be applicable to the real ocean if the model is sufficiently realistic. The ocean model horizontal resolution near the equator is near the low end of the resolution that is considered acceptable for equatorial wave simulation, especially for representing the equatorial Kelvin waves and for simulating the proper strength of equatorial upwelling. Results very similar to those discussed below were obtained using a 20-layer model with a higher horizontal resolution of 1.5° longitude and 0.5° latitude between 10°N and 10°S, decreasing to 1.5° latitude poleward of 20°. However, the control and backward experiments did not have identical heat flux formulations (see section 2b) in the higher-resolution experiments. The higher-resolution control experiment used a relaxation to the observed surface air temperature over the period of the integration, while the higher-resolution backward experiment used a relaxation to a climatological annual mean surface air temperature. Therefore, we will restrict the analysis to the more consistent set of low-resolution experiments in the following, while claiming that the resolution we are using is adequate for the purposes of this study.

b. Heat flux forcing

The parameterization of heat flux into the ocean can be thought of as a relaxation to an annual mean equilibrium air temperature. This form is used in order to help isolate changes caused by the variability of the surface wind stress. The heat flux is composed of radiative, sensible, and evaporative components. The solar radiation is prescribed over the basin as the annual mean climatology derived from the COADS (Comprehensive Ocean Atmosphere Data Set) data (Oberhuber 1988). The other components are parameterized as functions of the annual mean surface air temperature (Oort 1983). The formulation for longwave radiation is taken from Rosati and Miyakoda (1988), neglecting the effects of cloudiness. The sensible and latent heat fluxes are parameterized by bulk turbulent transfer formulas, with parameters as given by Philander and Pacanowski (1986). A relative humidity of 0.8 is used to calculate the evaporative heat flux. The surface wind speed for calculating the sensible and latent heat fluxes is determined from the prescribed wind stress forcing

using the bulk formula and a drag coefficient $c_D = 1.4 \times 10^{-3}$.

An additional damping of SST to annual mean surface air temperature is added to the heat flux forcing poleward of 20° latitude. The damping time is set to 50 days poleward of 30° latitude and behaves as (latitude − 20°)$^{-1}$ between 20° and 30° latitude.

We have determined that this heat flux formulation does not produce significant SST anomalies by itself, a behavior that could occur due to the dependence of the transfer coefficients on surface wind speed. The temperature dependence of the heat flux parameterization can be linearized, and the parameterization can written as a relaxation to a time-varying equilibrium temperature with a time constant that depends on wind speed. The equilibrium temperature can be determined by solving for the temperature at which the heat flux forcing is zero. This equilibrium temperature depends on the wind speed. It is warmer than the surface air temperature in the equatorial regions since the observed net radiative flux is into the ocean there. The dependence of the relaxation time constant and equilibrium temperature on surface wind speed will then cause SST variability through the heat flux parameterization. We have tested the importance of this effect by repeating the control experiment with the heat flux parameterized as a linear relaxation of the surface layer SST to the climatological annual mean surface air temperature with a proportionality constant of 45W (m^2 °C)$^{-1}$. The time constant for a 1°C temperature anomaly in a mixed layer 45 m deep to relax to the surface air temperature is about 40 days with this formulation. After the annual cycle was removed, there were no obvious significant differences between the results from this experiment and the control experiment. Therefore we interpret the anomalies in the experiments described below as being produced entirely by wind stress forcing, with the heat flux acting only to damp the anomalies.

c. *Salinity forcing*

Surface salinity is damped to its annual mean value (Levitus 1982) with damping time of 50 days poleward of 30° latitude and behaving as (latitude − 20°)$^{-1}$ between 20° and 30° latitude. No surface salinity damping is used equatorward of 20° latitude.

d. *Wind stress forcing*

The surface wind stress is calculated from four times daily European Centre for Medium-Range Weather Forecasts (ECMWF) 1986–1992 1000-mb winds using the drag coefficient formulation of Trenberth et al. (1990) in neutral conditions. Monthly mean stresses linearly interpolated to model grid point and time step are used to force the ocean models.

e. *Description of cases for the basic experiment*

The ocean initial conditions for each experiment were taken to be a state of rest with climatological January temperature and salinity (Levitus 1982). Then a periodic forcing using the monthly 1986–1992 wind stress climatology derived from the data series for the appropriate experiment (see below) was applied for four years in order to spin up the model. Thereafter, the actual wind stress for each month was used to obtain the results. The two cases to be described below are as follows:

- *Control*—the wind stress forcing as observed from January, 1986 through December, 1992 was applied directly to the ocean model. The monthly climatology of this forcing was used in the spinup phase.
- *Backward*—the wind stress forcing was the same as that applied to *Control* but reversed in time. That is, the initial condition wind stress after the spinup was taken from December 1992 observations. One simulated month later the forcing was from November 1992 observations and so on until the final month, which used the wind stress from January 1986. The climatological wind stress used in the spinup was also applied in reverse order from *Control* (December, November, October, . . .).

3. Results

A climatological annual cycle is defined separately for each experiment and for the observations. The climatology for each month is taken to be the average of the monthly mean values for the period of interest, 1986–1992. Anomalies are calculated for each case by removing its annual cycle. Then the *Control* anomaly is defined as the *Control* solution minus the *Control* annual cycle, the *Backward* anomaly is the *Backward* solution minus the *Backward* annual cycle, and the observed anomaly is the observed field minus the observed annual cycle. Results are presented for both SST and heat content anomalies, where heat content is defined as the average temperature in the upper 300 m of the ocean (approximately proportional to thermocline depth). The "time" axis is absolute only for observations and *Control.* In *Backward* the displayed time axis is the time the wind stress forcing was measured, which will be referred to as "forcing time." Real time (also referred to as model time) and forcing time are equivalent in observations and *Control.* Real time is reversed with respect to forcing time in *Backward.* Correlations are taken with reference to the forcing time coordinate. In forcing time the wind stress forcing applied in each experiment is identical and differences in the results must be due to time lags in the response to that forcing.

a. *Sea surface temperature anomalies*

The model simulation of the observed SST anomalies in the Pacific from January 1986 through December 1992 is shown in Fig. 1. *Control* produces a good simulation of the observed anomalies close to the

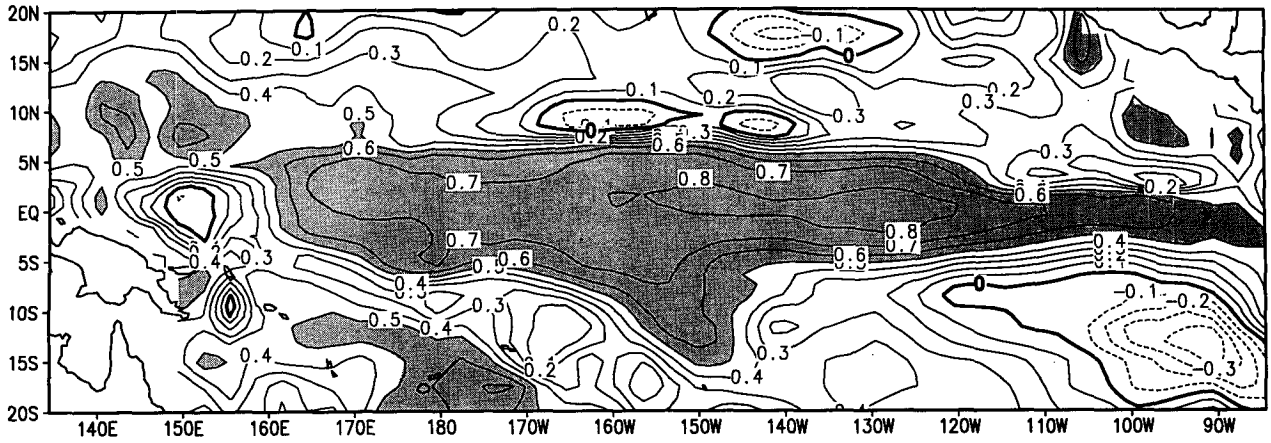

FIG. 1. Correlation of SST anomalies from annual cycle of *Control* (ocean model response to observed wind stress forcing) with observed SST anomalies. Contour interval is 0.1 with regions of correlation greater than 0.5 shaded.

equator. The performance of our model is comparable to that found from other ocean models (Miller et al. 1993). The anomaly correlations in Fig. 1 are very similar to those found using the same forcing in an ocean model version with approximately double the resolution in each direction, while the magnitudes of the SST anomalies are slightly lower for the lower-resolution model. The degradation of the simulation apparent in Fig. 1 in the equatorial eastern Pacific appears to be property of the GFDL model—for example, Miller et al. (1993) show that the Lamont ocean model forced by observed wind stress has its highest anomaly correlations in the eastern equatorial Pacific. The regions in our domain of interest where the correlations are poorest, the central Pacific near 7°N, the eastern Pacific near 10°S, and the equator near 150°E, are all regions of small SST anomalies in both the observations and the model. Therefore, the model is doing an adequate job of simulating the observations in these areas for our purposes, and the poor correlations there are probably not important.

Figure 2 shows the time series of equatorial SST anomalies for observations, *Control,* and *Backward.* The significant events that occurred in the 1986–1992 time period are El Niño (warm) events in 1986–1987 and 1991–1992 and a La Niña (cold) episode in 1988–1989. As can be seen from Fig. 2, most of the variance in SST anomalies occurs on interannual timescales in both the model and observation. Agreement between *Control* and observations along the equator is good, except in the far western Pacific, where the simulated anomalies are too large, and the far eastern Pacific, where the simulated anomalies are too small. The observed and simulated equatorial SST anomalies show little evidence of systematic east–west propagation. This period differs from the 1967–1978 time period studied by Chao and Philander (1993), during which the equatorial SST anomalies appeared to have a systematic westward propagation in the central Pacific. We conclude from Figs. 1 and 2 that the ocean model has adequate resolution and a suitable configuration to simulate the observed interannual variability of SST over most of the equatorial Pacific Ocean with prescribed wind stress forcing. Apparently errors in the simulation of equatorial SST in the far eastern and far western Pacific do little to degrade the quality of the simulation in the central Pacific.

The equatorial SST anomalies of *Control* and *Backward* shown in Fig. 2 have much in common. Both simulations capture the observed sequence and structure of the observed warm and cold events. Some differences are also apparent, especially a later decay of the 1987 El Niño, a later onset of the 1989 La Niña, and a slower decay of the cold event in *Backward.* Figure 3 shows that in forcing time the *Control* and *Backward* solutions for SST are very similar over much of the basin. The solutions begin to differ over the equatorial eastern Pacific and the western south Pacific. Compared to the observations *Backward* performs nearly as well as *Control* where the correlations in Fig. 3 are high but is significantly worse where the correlations are smaller. It should be noted that poor correlations in the far western equatorial Pacific are common to both Figs. 1 and 3.

We interpret the region of very high correlation in Fig. 3, which at the equator extends from about 160°E to 160°W, as regions where the model SST is approximately in equilibrium with the wind stress forcing. In regions of lower correlation, memory effects and time lags due either to wave propagation in the thermocline, heat storage in the mixed layer, or some other effect must be of increasing importance, and the response is not in equilibrium with the wind stress forcing. In those regions of high correlation in Fig. 3 where *Control* also produces a good simulation of the observations, especially the west-central equatorial Pacific region mentioned above, we infer that the actual Pacific Ocean SST anomalies are approximately in equilibrium with

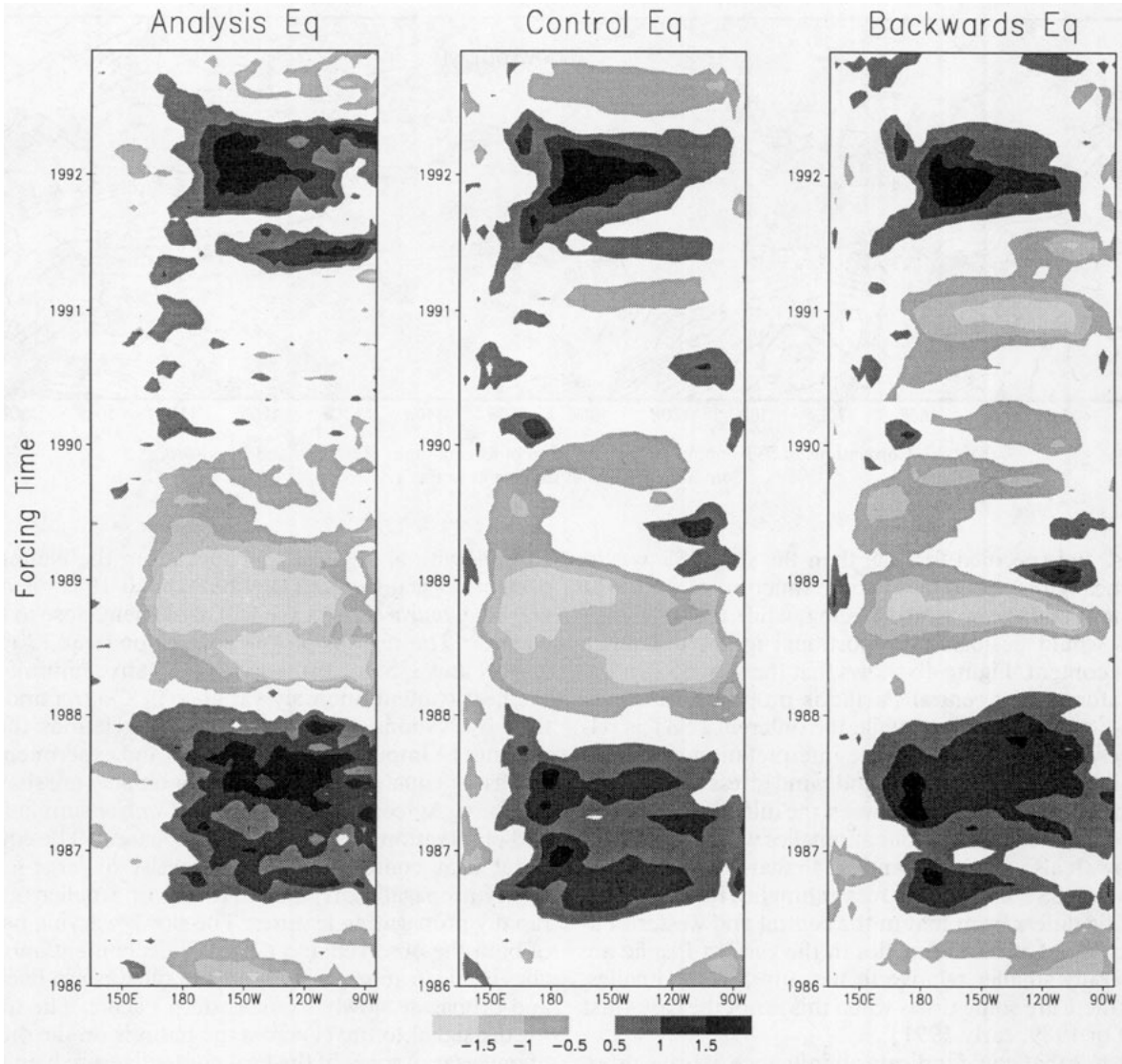

FIG. 2. Time series of equatorial SST anomalies (°C) for observations (left), *Control* (center), and *Backward* (reversed forcing case, right). The time axis is real time for observations and *Control*. The time axis for *Backward* refers to the time the wind stress forcing was measured. The time integration for *Backward* started at the top of the figure and ended at the bottom.

the wind stress forcing. In order for the SST anomalies to be in equilibrium with the forcing, both anomalous heat storage in the surface layer and the influence of subsurface heat content anomalies, if these are not in equilibrium, need to be relatively small terms in the heat budget. A comprehensive analysis of the anomalous heat budget of the upper 45 m of the equatorial Pacific of an extended control simulation (Huang and Schneider 1995) verifies that this is indeed the case. West of about 150°W the anomalous heat budget is an approximate balance between surface heat flux and advection by anomalous zonal currents acting on the time-mean longitudinal temperature gradient. When the wind stress anomaly is positive, SST anomalies are positive, so that the net heat flux is into the ocean, giving anomalous cooling ($Q' < 0$). Additionally, the anomalous surface layer zonal velocity u' is approximately in equilibrium with the wind stress ($u' > 0$) and acts on an annual mean temperature $[T]$ that decreases toward the east ($\partial[T]/\partial x < 0$), so that $u'\partial[T]/\partial x < 0$ and balances Q'. The advection and heat flux terms change sign when the anomalous wind stress is negative.

Figure 4a displays the relationship between the sum (half of *Control* plus *Backward*) and difference (half of *Control* minus *Backward*) equatorial SST of the two experiments. The difference tends to be small compared to the sum except in the eastern Pacific. If the SST budget was a linear local in space equilibrium relationship between SST anomalies, heat content anom-

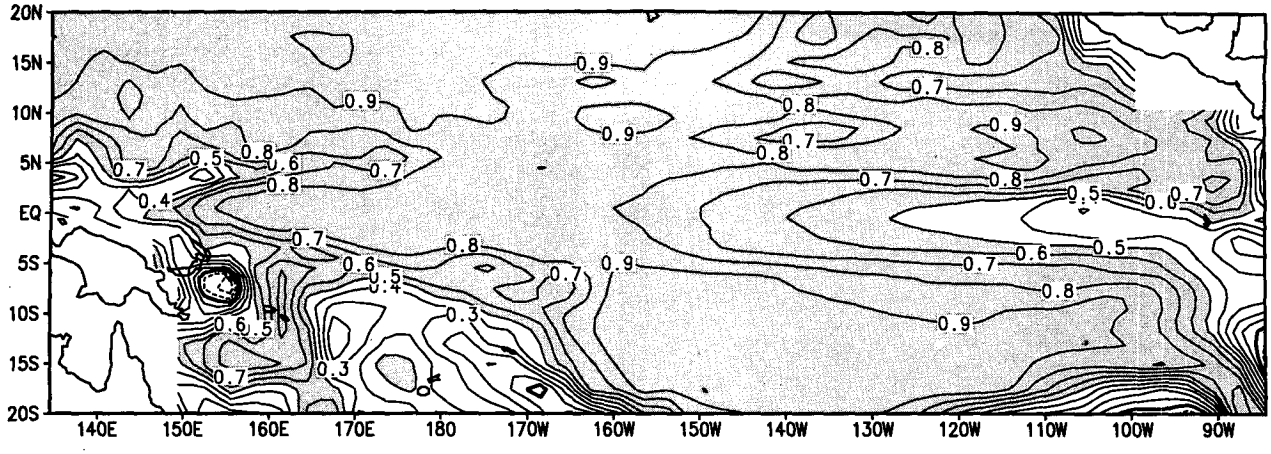

FIG. 3. Correlations of SST anomalies (as a function of forcing-time) of *Control* and *Backward*. Contour interval and shading as in Fig. 1.

alies, and specified forcing, then the sum SST would be locally proportional to some function of sum heat content and the specified forcing, while the difference SST would be locally proportional to the difference heat content. Figure 4b shows that the sum SST in the equatorial west-central Pacific is proportional to the wind stress anomalies, while the difference SST is relatively small, supporting the interpretation of a local equilibrium between SST and wind stress in these regions. The relationship between the difference SST and the difference heat content anomalies will be examined below. It also appears from Fig. 4b that the relationship between SST and wind stress anomalies in the eastern Pacific differs from that in the central and western Pacific. Wind stress anomalies in the eastern Pacific are generally smaller relative to the sum SST anomalies, but there are some times when this is not the case (first half of 1989, early 1991).

A test that could indicate an influence of wave propagation on the SST is to compute the lag correlation with respect to forcing time between the SSTs of *Control* and *Backward*. If the SST in a region is influenced primarily by disturbances propagating from some remote forcing region, then the influence will be felt after the forcing is applied in *Control* but will be felt before (in forcing time) the forcing occurs in *Backward*. In this situation, the largest correlation between the SSTs in the remotely forced region in the two experiments would occur when *Control* lags *Backward*. However, when the test is applied the lag correlations show no sign of this behavior—the maximum correlations of SST occur at zero lag and decay monotonically as the lag increases.

b. Heat content anomalies

The ability of the *Control* simulation to reproduce the observed 1986–1992 heat content anomalies in the Pacific is shown in Fig. 5, in which the correlation of *Control* with an analysis obtained from the National Meteorological Center (Leetmaa and Ji 1989) is displayed. *Control* shows excellent agreement close to the equator. The regions of low correlation near 170°W at 3°N and 3°S are also regions of relative minima in the heat content anomaly variance in *Control* and in the observations, so that the poor correlations there may not be important. The observed and experimental results for equatorial heat content anomalies are shown in Fig. 6. Agreement between the *Control* simulation and observations at the equator is apparent. The equatorial heat content anomalies consist of large-scale slowly propagating regions that contain smaller more rapidly propagating features. The slowly varying parts of both the observed and *Control* heat content anomalies in Fig. 6 appear to originate in the western Pacific and propagate slowly to the eastern Pacific. The time for the signal to travel across the basin is on the order of one year. Arrival of the heat content anomaly in the eastern Pacific coincides with the mature phase of the warm or cold event in SST, with heat content and SST anomalies having the same sign at those times.

Comparison of the equatorial heat content anomalies of *Control* and *Backward* gives an entirely different picture from the comparison of SST anomalies. While good agreement between the SST anomalies of *Control* and *Backward* is obvious in Fig. 2, serious disagreement between the heat content anomalies is evident in Fig. 6. In *Control* there is pronounced eastward propagation in time, while in *Backward* the direction of propagation is westward in forcing-time (but also eastward in real time, which proceeds from top to bottom in the right-hand panel), and there is little apparent agreement between the sign of the anomalies at any longitude.

The prominent systematic slow eastward propagation in real time of heat content anomalies shown in Fig. 6 is evidence that the heat content anomalies are not in equilibrium with the wind stress forcing. If the heat content anomalies were in equilibrium with the

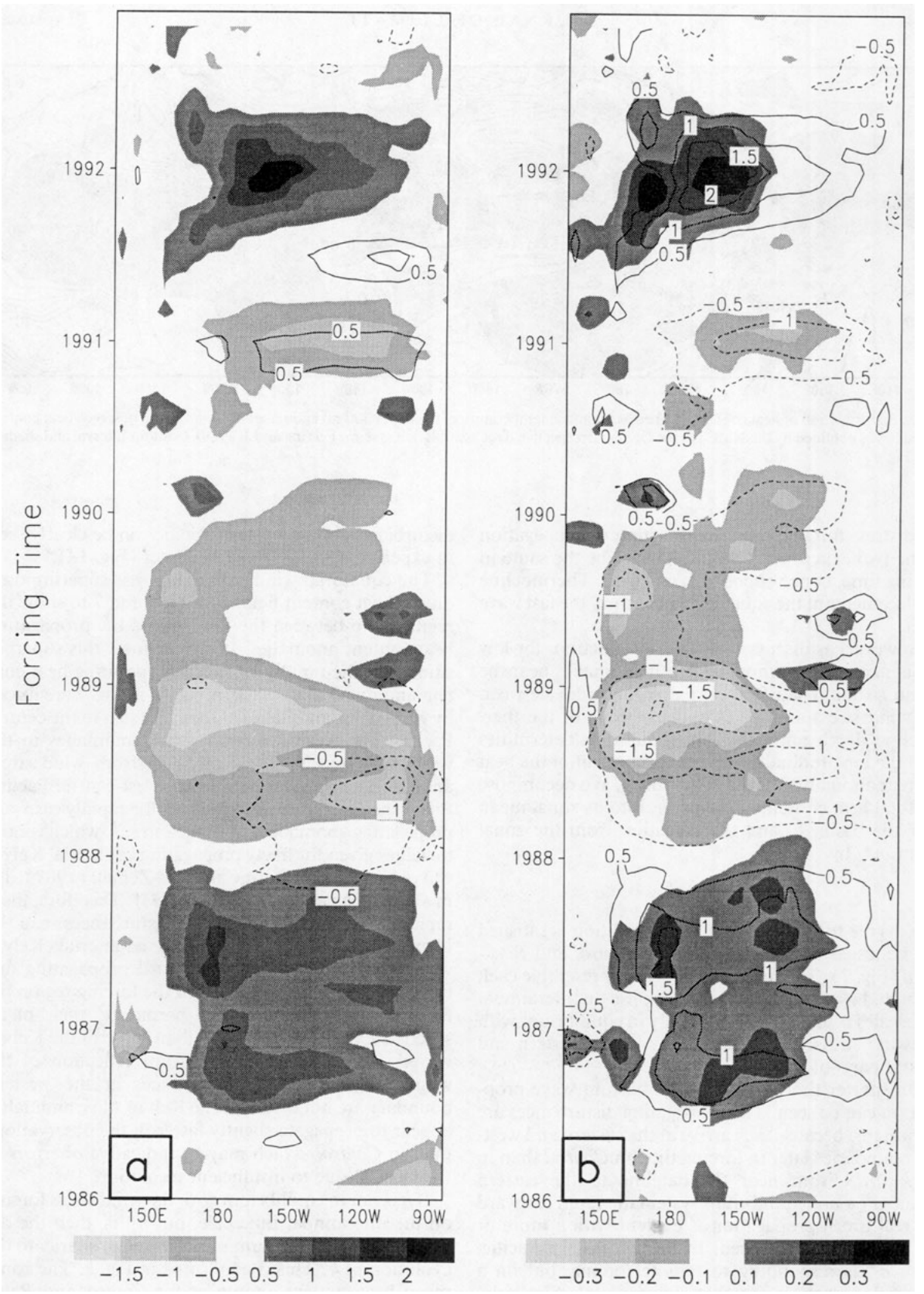

FIG. 4. (a) Sum (one-half of *Control* plus *Backward*) and difference (one-half of *Control* minus *Backward*) of the equatorial SST anomalies. The sum is shown by the shading, while the difference is shown by the superimposed contours. (b) Zonal wind stress anomalies at the equator (dyn cm^{-2}, shading) and sum (one-half of *Control* plus *Backward*) of the equatorial SST anomalies (contours). Contour interval is 0.5°C for temperatures and the zero contour is suppressed. The wind stress plot has been smoothed using a nine-point space-time smoother.

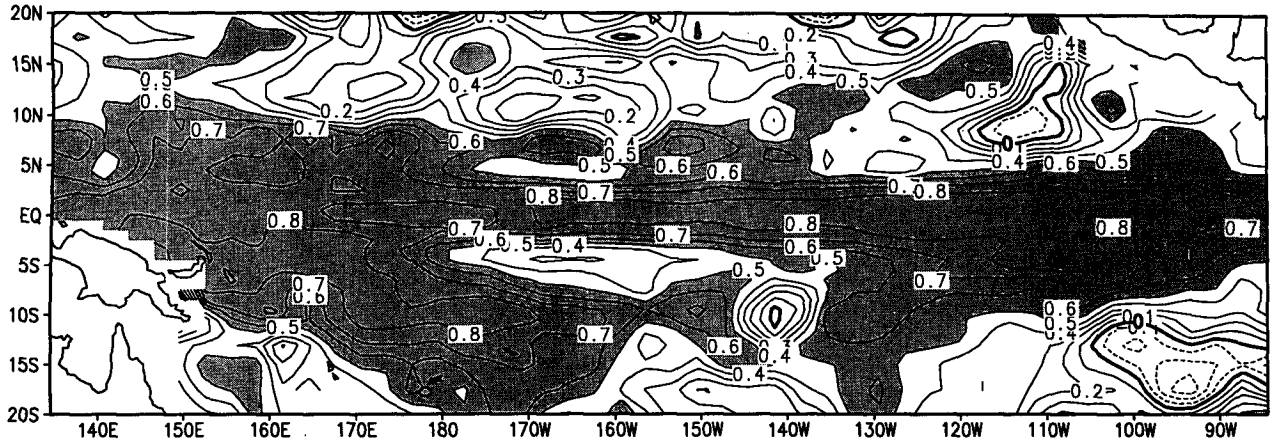

FIG. 5. Correlation of heat content (defined as the mean temperature of the upper 300 m) anomalies of *Control* with observed heat content anomalies as obtained by the NMC Pacific Ocean retrospective data-assimilation system (Leetma and Ji 1989). Contour interval and shading as in Fig. 1.

wind stress forcing, then the direction of propagation in the two experiments would have to be the same in forcing time, hence opposite in real time. Thermocline displacements at the equator do not satisfy the fast wave limit.

However, as discussed in the introduction, for low frequencies the thermocline depth anomalies near the equator should satisfy a partial equilibrium between the wind stress anomalies and the slope of the thermocline depth anomaly. This condition determines only the longitudinally varying component of the heat content anomaly, not the zonal mean. We decompose the total heat content anomaly, h, into its zonal mean over the basin, $\bar{h}$, and the deviation from the zonal mean, h^*, by

$$h = h^* + \bar{h}.$$

The degree to which the balance condition is satisfied can be tested by comparing h^* of *Control* and *Backward* (Fig. 7). The results for h^* closely resemble each other and we infer that the h^* response on interannual timescales *is* in fact approximately in equilibrium with the wind stress forcing, especially in the western and central parts of the basin.

On shorter timescales, nonequilibrium wave propagation can be seen. The propagating disturbances are identifiable because they arrive at the eastern and western boundaries later in forcing time in *Control* than in *Backward*. From near the dateline to the eastern boundary a nonequilibrium systematic rapid eastward (in real time) propagation is evident with a more or less uniform phase speed. In the far eastern Pacific, then, h^* is responding to remote forcing, but on a timescale much faster than interannual. Similarly, westward propagation in real time can be seen, although not as clearly, from near the dateline to the western boundary. However, westward propagating disturbances in the western Pacific can be clearly seen in experiments to be described later (Fig. 14).

The equatorial wind stress forcing is superimposed on the heat content fields in Figs. 6 and 7 to show the relationship between the forcing and the propagating heat content anomalies. It is clear from this superposition that the rapidly eastward propagating heat content anomalies in the eastern Pacific in Fig. 7 are forced by wind stress anomalies of the same sign in the central Pacific. The westward propagating anomalies in the western Pacific in Fig. 7 originate from wind stress anomalies of opposite sign in the west-central Pacific. Phase speeds crudely estimated for the rapidly eastward propagating anomalies are about 2 m s^{-1}, which is close to values given for freely propagating equatorial Kelvin waves [2.75 m s^{-1} from Cane and Zebiak (1987); 1.5 m s^{-1} in Chao and Philander (1993)]. Therefore, these rapidly eastward propagating disturbances can be identified as freely propagating equatorial Kelvin waves. As the apparently westward propagating disturbances do not travel far from the forcing region before they reach the western boundary, their phase speeds are less clearly defined than those of the Kelvin waves. Kelvin waves arising from reflection of the westward propagating disturbances at the western boundary are not evident. The Kelvin wave anomalies appear to propagate slightly faster in the observations than in *Control*, which may be indicative of errors in the OGCM due to insufficient resolution.

If h is not in equilibrium with the wind stress forcing on the interannual timescale, but h^* is, then the departure from equilibrium must be due primarily to the evolution of $\bar{h}$. This is confirmed in Fig. 8. The zonal mean heat content anomalies for *Control* and *Backward* tend to be of opposite sign when viewed as a function of forcing time (correlation −0.48). Also, the zonal mean equatorial heat content decreases during

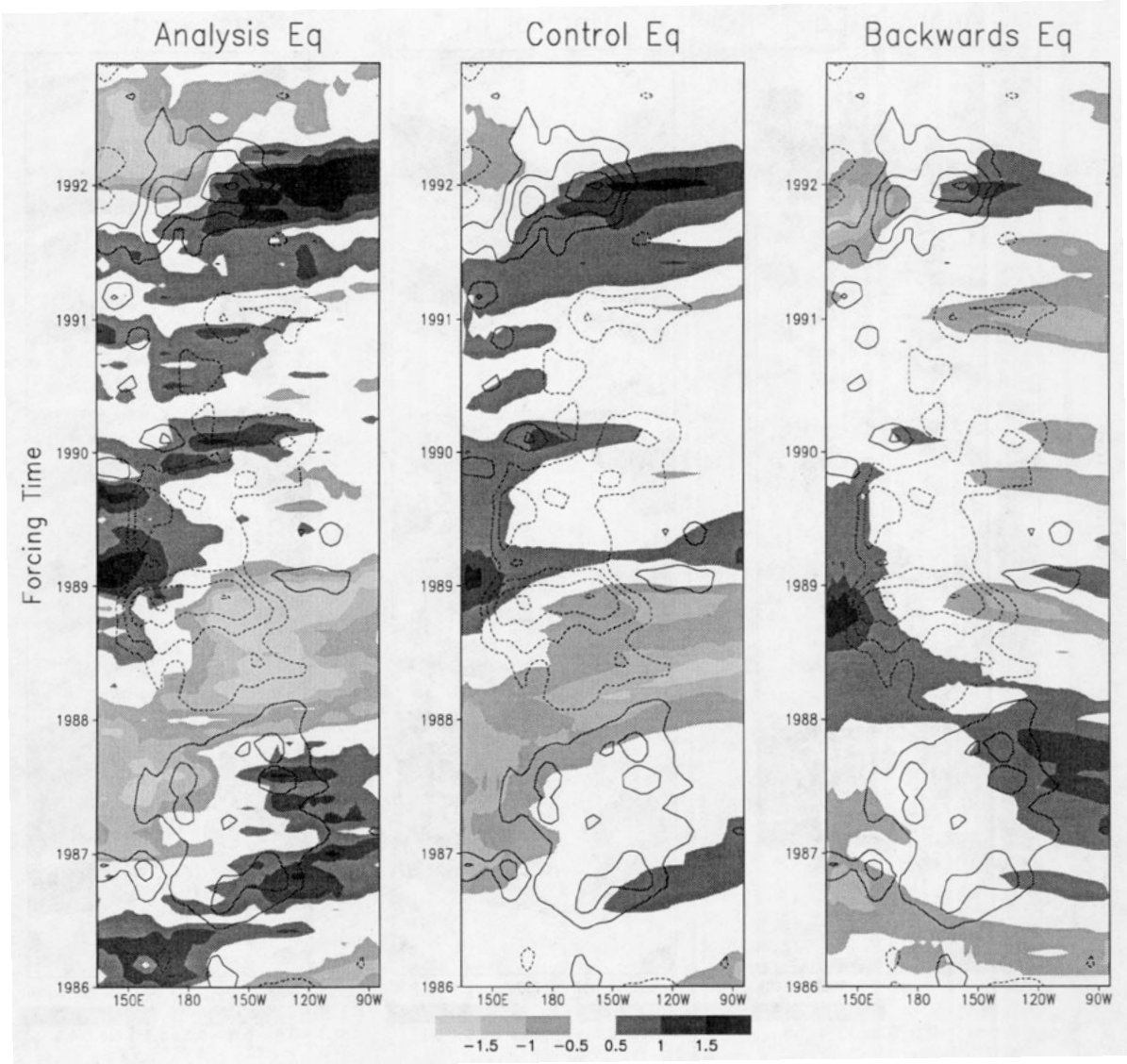

FIG. 6. Time series of equatorial heat content anomalies (°C, shaded) as obtained by the NMC Pacific Ocean retrospective data-assimilation system (left, Leetma and Ji 1989), *Control* (center), and *Backward* (right). The superimposed contours in each panel are the smoothed equatorial wind stress anomalies, contour interval 0.1 dyn, zero contour suppressed (cf. Fig. 4b).

El Niño events when considered as a function of real time for both cases (real time increasing from left to right for *Control* and from right to left for *Backward* in Fig. 8). This association between equatorial heat content tendency and El Niño events agrees with the results of Wyrtki (1985), Zebiak and Cane (1987), Philander and Hurlin (1988), and Zebiak (1989). The zonal mean heat content anomalies are clearly *not* in equilibrium with the wind stress forcing. The ocean model's zonal mean heat content anomalies contain information (memory) concerning the prior history of the slowly varying components of the forcing.

The horizontal structure of the correlations in forcing time between the heat content anomalies of *Control* and *Backward* is presented in Fig. 9. The correlations of the total heat content anomalies (Fig. 9a) are very low or negative within about 3° latitude of the equator. Narrow zonally oriented bands in which the two simulations are well correlated flank the equatorial low-correlation region near the date line. Heat content anomalies are in equilibrium with the wind stress forcing in these bands but not along the equator. When the zonal mean heat content is removed and the correlations are calculated (Fig. 9b) the equatorial values increase remarkably, exceeding 0.8 over much of the equatorial Pacific. The removal of the zonal mean increases the correlations primarily in the equatorial low-correlation band of Fig. 9a. There is little change of the correlation in the high-correlation bands that flank the equa-

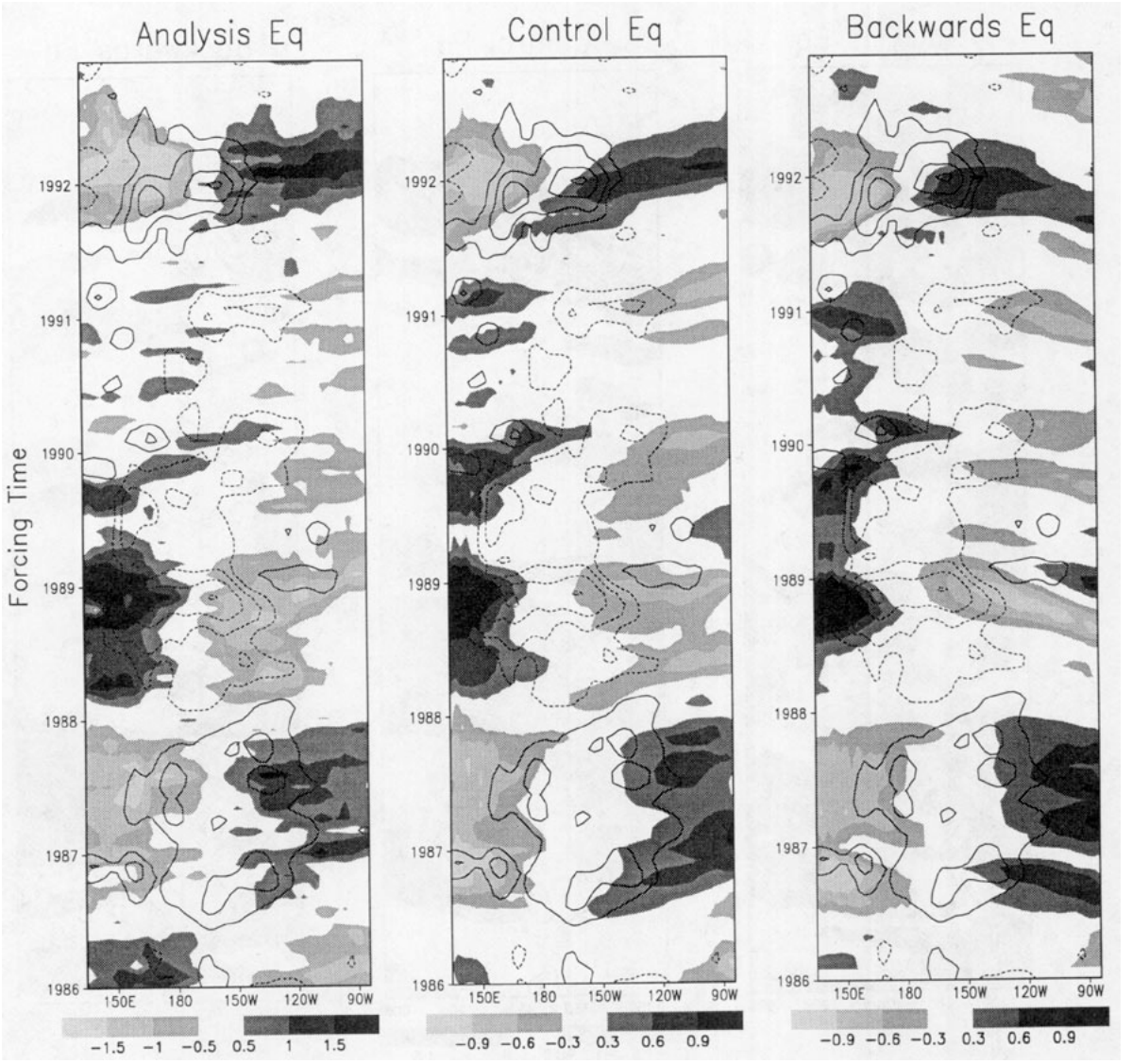

FIG. 7. Time series of equatorial heat content anomalies with the longitudinal means over the basin removed (°C, shaded) for observations (left), *Control* (center), and *Backward* (right). The superimposed contours in each panel are the smoothed equatorial wind stress anomalies, contour interval 0.1 dyn, zero contour suppressed (cf. Fig. 4b).

tor in Fig. 9a or in the far eastern equatorial Pacific.

The analysis shows that on interannual timescales h^* in the model equatorial Pacific is to a first approximation independent of the previous history of the wind stress forcing when observed wind stress forcing for 1986–1992 is used. The power in the observed forcing is contained in long enough timescales so that h^* remains in equilibrium with the forcing in the equatorial waveguide. However, the equilibrium applies only to h^*, but not to $\bar{h}$ or h, and the model does not satisfy the fast wave limit.

c. *Heat content anomalies off the equator*

The heat content anomalies for the analysis, *Control,* and *Backward* are shown at 5°N in Fig. 10 and at 7.5°S in Fig. 11, with equatorial wind stress anomalies contours superimposed. Equatorial wind stress anomalies show a clear association with these off-equator heat content anomalies. Westward propagating anomalies in real time are seen to originate in the western and west-central Pacific, more or less symmetrically about the equator. The anomalies in *Control* and *Backward* are similar near the longitudes of strong wind stress forcing, corresponding to the regions of high correlation in Fig. 9a, but separate from each other going toward the western boundary. The systematic westward propagation in both experiments proves that the heat content anomalies in the western Pacific off the equator are not in equilibrium with the wind stress forcing. However, the propagation timescales appear to be short relative to the timescale of the interannual variability.

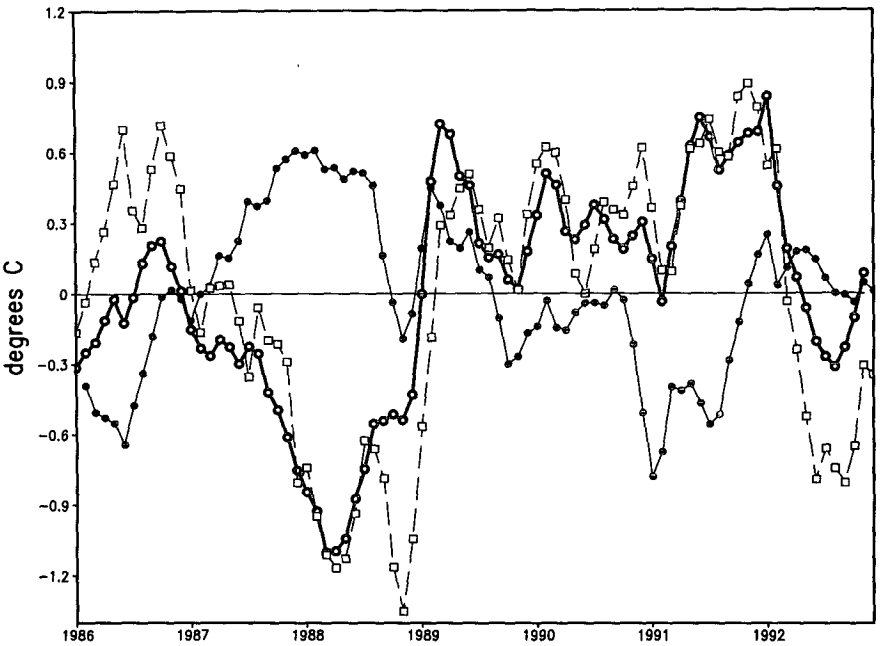

FIG. 8. Time series of longitudinal mean over the Pacific basin of equatorial heat content anomalies for *Control* (darker line, open circles), *Backward* (lighter line, filled circles), and observations (dashed line, open squares).

The propagation speed of these heat content anomalies is estimated to be about 0.5 m s^{-1}, which is about one-third of the Kelvin wave speed and identifies the anomalies as more or less freely propagating low-order Rossby waves. The westward propagating anomalies at the equator are closely related to these off-equatorial features and also may be identified as Rossby waves.

The arrival of these Rossby waves at the western boundary occurs at about the same time both off and on the equator. The difference in arrival time at 5°N between *Control* and *Backward* appears to be about one year for disturbances originating in the central Pacific and much less for disturbances forced in the western Pacific. The off-equatorial bands of high correlation in Fig. 9a can be interpreted as the regions where these Rossby waves are forced. The westward propagation produces a the decay of correlation between *Control* and *Backward* between the central and western Pacific in Fig. 9a. The slowly eastward propagating equatorial heat content anomalies of *Control* and *Backward* near the western boundary appear to originate when the Rossby waves reach the western boundary. The correspondence between observation and *Control* supports this Rossby wave interpretation for the real ocean.

Very slow westward propagating disturbances can be seen near the eastern boundary in the model results in Figs. 10 and 11. They would take three years or longer to cross the basin, but they disappear by 120°W. Comparison with Fig. 6 shows that these disturbances are the reflections of the Kelvin wave heat content anomalies incident on the eastern boundary. The slow westward phase speed suggests these may be Rossby waves with smaller equivalent depths than those forced by the wind stress to the west. The numerical experiments are not long enough to diagnose the role of these slow eastern Pacific Rossby waves in the coupled system.

d. Relationship between equatorial heat content and SST anomalies

A relationship between the heat content and SST anomalies is seen in Fig. 12, which superimposes the equatorial difference (one-half of *Control* minus *Backward*) SST anomalies on the equatorial difference heat content anomalies. The difference heat content anomalies have relatively little longitude dependence and have a strong low-frequency component. A zonally uniform difference heat content is the expected result if the approximate equilibrium between wind stress and thermocline slope is holding. The difference heat content anomalies represent a part of the model response that is not in equilibrium with the wind stress forcing. The difference SST was interpreted above as a part of the SST response not in equilibrium with the wind stress forcing. Clearly, however, the difference SST is closely related to the difference heat content. The sign of the difference heat content anomalies and SST anomalies is the same, and the sensitivity of the difference SST to the difference heat content appears to increase toward the east. The relationship between the difference anomalies of heat content and SST in the

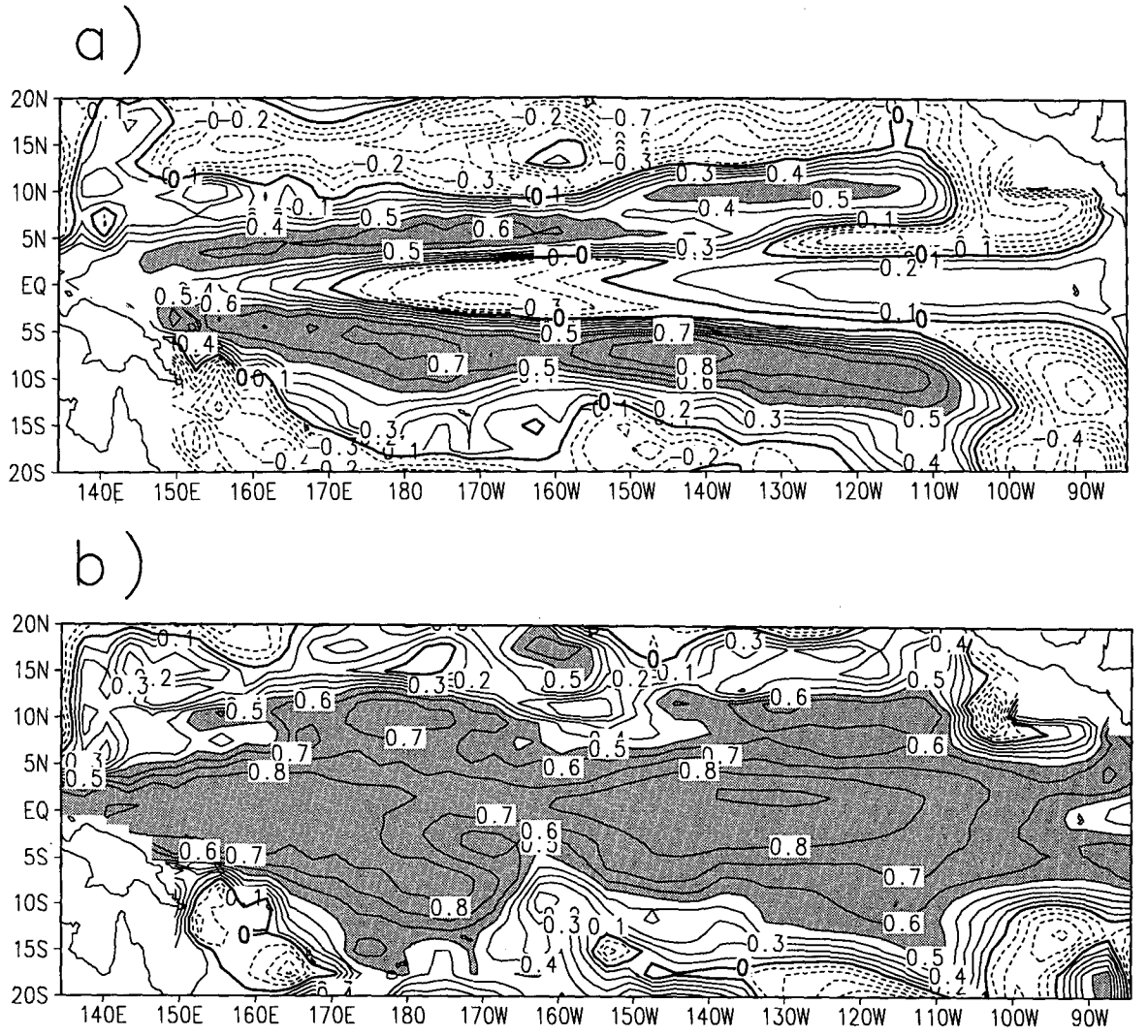

FIG. 9. (a) Correlations in forcing time between heat content anomalies of *Control* and *Backward*. (b) As in (a) but for heat content anomalies with the zonal mean removed. Contour interval and shading as in Fig. 1.

eastern Pacific shown in Figs. 4 and 11 is consistent with the SST being in a local equilibrium with surface heat flux forcing and heat content as discussed in section 3a. This is the fast SST limit. The heat budget of Huang and Schneider (1995) shows that the dominant terms in the SST budget to the east of about 110°W are anomalous heat flux and anomalous vertical advection by the mean vertical velocity.

4. Interpretation

We have pointed out above that the time lag between the *Control* and *Backward* heat content anomalies is such that they appear to be almost 180° out of phase (Fig. 8). This somewhat mysterious result would seem at first sight to imply time lags in the system on the order of years, much longer than wave-transit times. In this section some additional experiments are performed to isolate the physically important time lags. These experiments, together with *Control* and *Backward*, show that the physically relevant delay time is the time it takes a free Rossby wave to propagate from the forcing region to the western boundary. This delay, together with the equilibrium of the thermocline slope with the wind stress, can explain the behavior of the equatorial mean heat content. The results from the experiments are used to determine the parameters of an empirical time delay equation for the response of the equatorial heat content to wind stress forcing.

The time-delay equation is shown to be consistent with low-frequency oscillatory coupled instabilities in the fast-SST limit diagnosed from the OGCM. The two necessary ingredients for the low-frequency unstable oscillations in this system are shown to be 1) the time

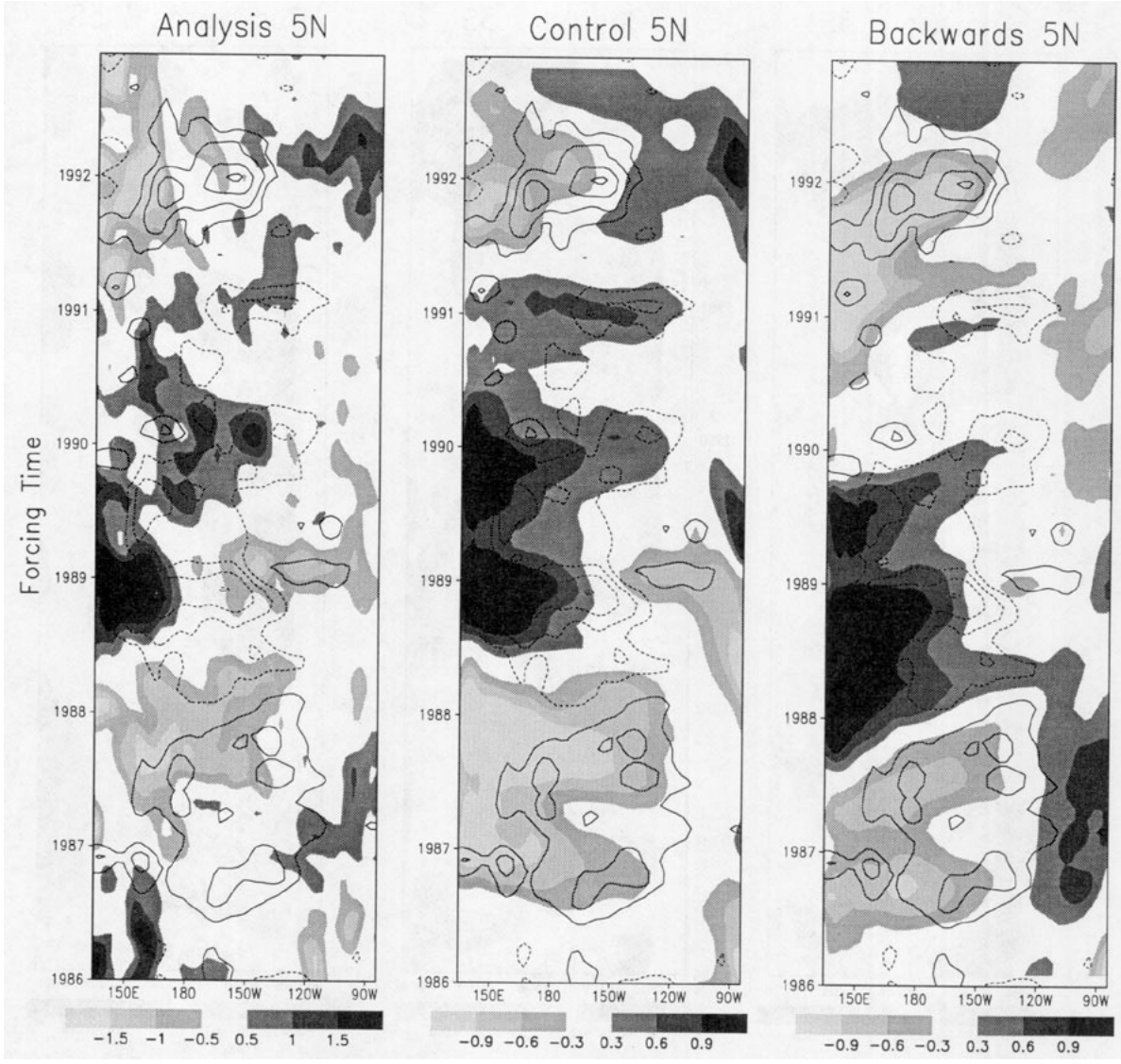

FIG. 10. Time series of heat content anomalies at 5°N (°C, shaded) as obtained by the NMC Pacific Ocean retrospective data-assimilation system (left, Leetma and Ji 1989), *Control* (center), and *Backward* (right). The superimposed contours in each panel are the equatorial wind stress anomalies (cf. Fig. 4b), contour interval 0.1 dyn, zero contour suppressed. A nine-point space–time smoother has been applied to all of the plotted fields.

lag and 2) the frequency dependence of the heat content response at the western boundary. The results contained in this section appear to be described by dynamics contained in the linear forced shallow water equations and therefore should be consistent with known results from this system of equations such as those described by Cane and Sarachik (1981), Battisti and Hirst (1989), Schopf and Suarez (1990), and Cane et al. (1990).

a. Role of Rossby wave propagation

To identify time lags between heat content and wind stress forcing, the OGCM response was found to observed wind stress forcing whose time evolution was further distorted. In experiment *Fast* the evolution of the wind stress forcing (anomalies + annual cycle) was sped up by a factor of 3 that the wind stress went through its annual cycle in four months, comparable to the Kelvin wave basin crossing time. In experiment *Slow* the evolution of the wind stress was slowed down by a factor of 2 relative to *Control*. The backward version of both of these experiments, called *Fast Backward* and *Slow Backward* in the following were also performed. Anomalies were calculated with respect to the annual cycle of each experiment and compared in forcing time.

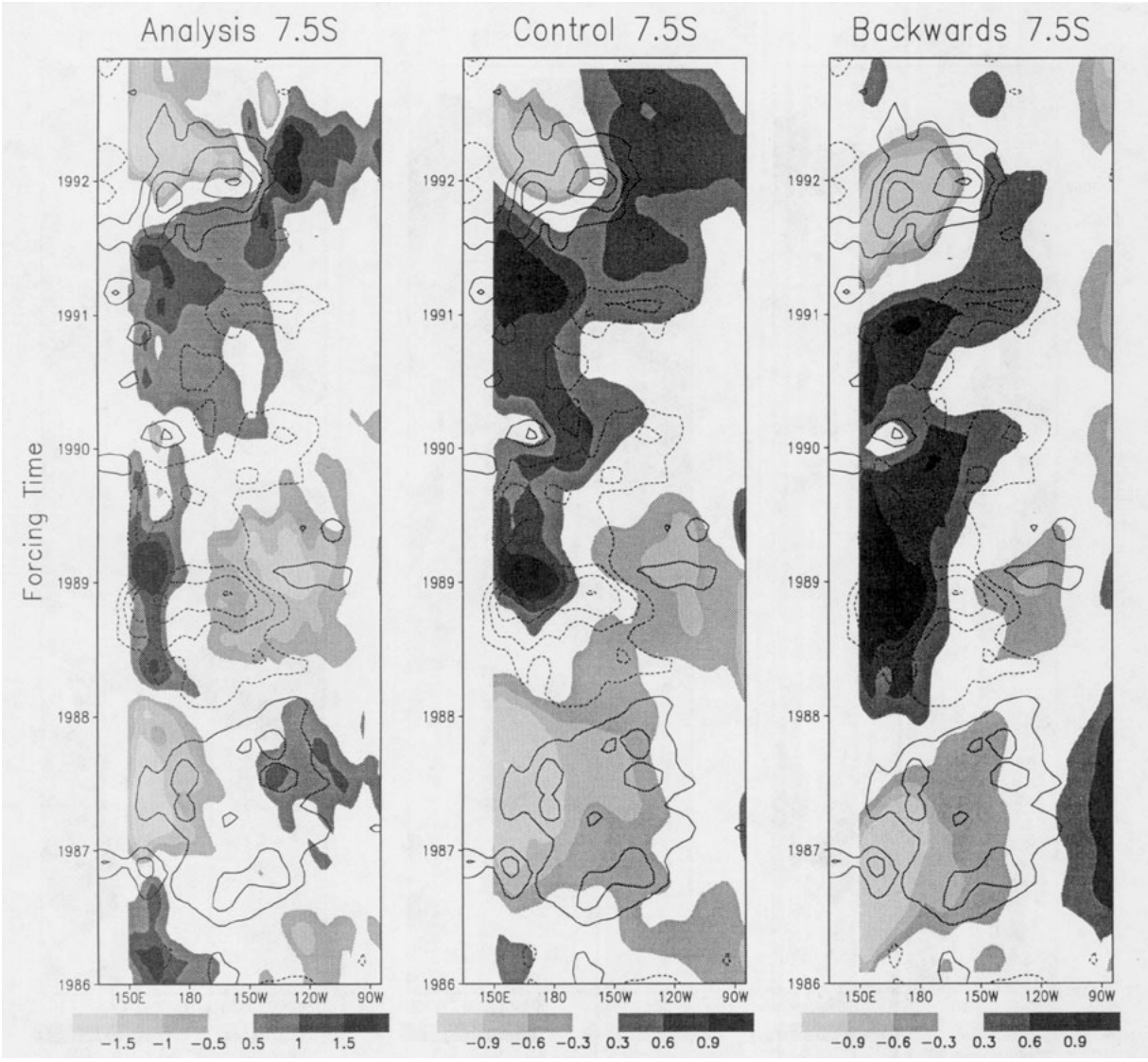

FIG. 11. Time series of heat content anomalies at 7.5°S (°C, shaded) as obtained by the NMC Pacific Ocean retrospective data-assimilation system (left, Leetma and Ji 1989), *Control* (center), and *Backward* (right). The superimposed contours in each panel are the equatorial wind stress anomalies (cf. Fig. 4b), contour interval 0.1 dyn, zero contour suppressed. A nine-point space–time smoother has been applied to all of the plotted fields.

If there are time lags between the wind stress forcing and the heat content response related to the phase propagation of ocean waves, then these time lags as seen in forcing time should be proportional to the factor multiplying the speed of the evolution of the forcing. That is, the time lag in *Slow* should be one-half of the time lag in *Control,* while the time lag in *Fast* should be three times the time lag in *Control.* In the three reversed forcing cases the time lags should appear as time leads in forcing time.

The evolution of the heat contents of *Slow, Control,* and *Fast* are compared at the equator (Fig. 13) and 5°N (Fig. 14). As the time evolution is sped up there appears to be an increase in the delay between the central Pacific and the eastern boundary at the equator and a longer time delay between the western boundary and the central Pacific at 5°N. Figure 14 shows heat content anomalies apparently forced by the equatorial wind stress anomalies and propagating to the western boundary. The westward propagating heat content anomalies are of opposite sign from the equatorial wind stress anomalies that apparently force them. The estimated phase speed, on the order of 0.5 m s^{-1} for all cases in model time, is appropriate for free Rossby waves. The equatorial heat content at the western boundary is highly simultaneously correlated with the off-equatorial heat content at the western boundary. The results suggest that the total heat content at the western boundary at the equator is determined by Rossby waves propagating westward from the forcing

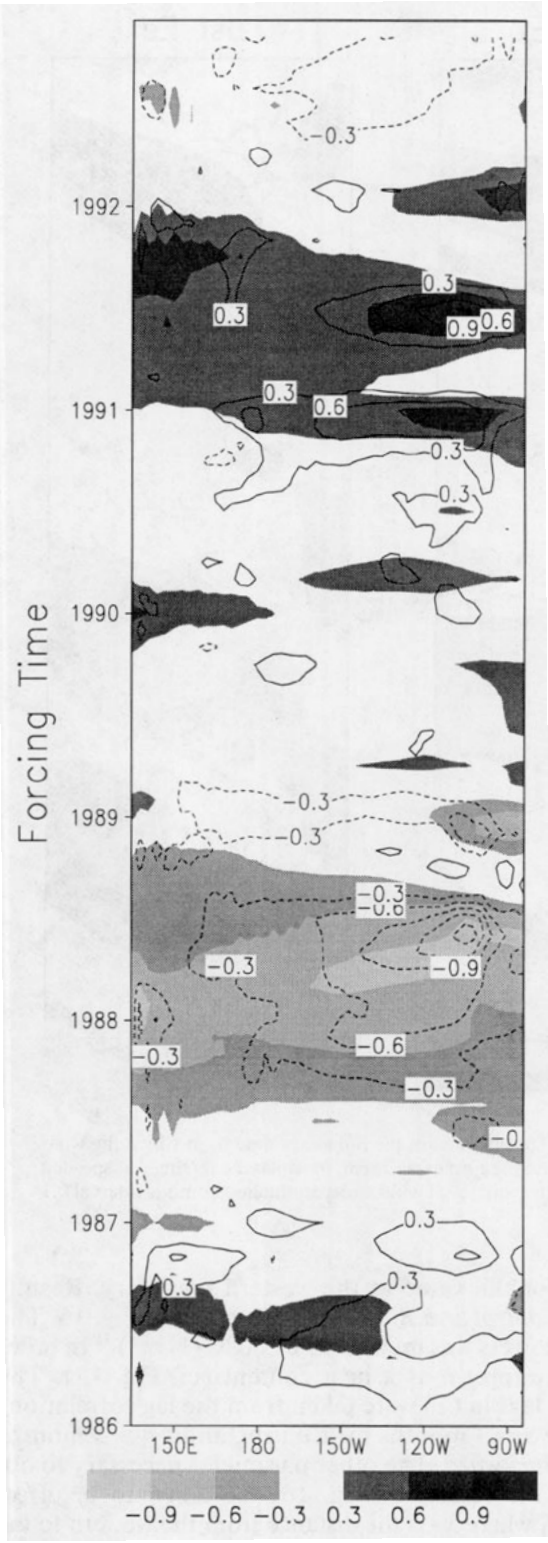

FIG. 12. Difference (one-half of *Control* minus *Backward*) equatorial heat content anomalies (°C, shaded). Difference (one-half of *Control* minus *Backward*) equatorial SST anomalies (contours, cf. Fig. 4a). Contour interval 0.3°C, zero contour suppressed.

region where they are produced by the curl of the wind stress.

Time lags between the wind stress forcing and western boundary response at the equator are demonstrated in Figs. 15a–c. There the time evolution of the mean wind stress at the equator averaged across the Pacific from 120°E to 80°W is compared to the time evolution of the equatorial heat content anomaly at the western boundary of the ocean model. A separate panel is shown for each pair of forward–backward experiments. A linear trend in model time in equatorial heat content, estimated at 0.095°C mo^{-1}, became evident in the *Slow* cases. This trend was removed in model time from all of the results shown in Fig. 15. The negative of the heat content at the western boundary, $-h_w$, is well described as the time-lagged response to this wind stress forcing. The wind stress forcing always leads $-h_w$ in model time (lagging in forcing time for the *Backward* cases). Figure 15 also shows that amplitude of the heat content response at the western boundary decreases as the magnitude of the frequency of the forcing increases, that is, proceeding from the slowed-down forcing cases to the sped-up cases. This behavior may have important consequences, as is shown below.

The time lags in forcing time have been estimated as the lag in integer months for which the maximum lag correlation between the equatorial mean wind stress and $-h_w$ shown in Fig. 15 occur. The maximum lag correlation is order 0.8 in each case and not sharply peaked. By this measure, the forcing leads $-h_w$ by three months in *Control* and lags $-h_w$ by three months in *Backward,* leads $-h_w$ by one month in *Slow* and lags $-h_w$ by one month in *Slow Backward*, and leads $-h_w$ by six months in *Fast* and lags $-h_w$ by seven months in *Fast Backward.* The time lags estimated from the lag correlations are consistent with h_w being determined by the wind stress forcing in the central Pacific and then propagating as free Rossby waves from the forcing region to the western boundary.

Using h_w now to represent the departure of the thermocline depth at the equatorial western boundary from H, the results show that in model time

$$h_w = -\frac{A}{\rho g H}\overline{\tau_x}(t - s), \qquad (1)$$

where τ_x is the zonal wind stress at the equator, the overbar indicates the longitudinal mean taken across the ocean basin, t is time, s is the time lag, A is a yet to be determined real positive constant with units of length, ρ is the density, and g is the effective gravitational acceleration. Equation (1) probably works well diagnostically because the large zonal wind stress anomalies are confined to a relatively narrow band of longitudes in the central Pacific (Fig. 4b), so that the delay time s is the Rossby wave travel time from this region to the western boundary.

It has been shown above that at the equator the heat content with the zonal mean removed is in equilibrium

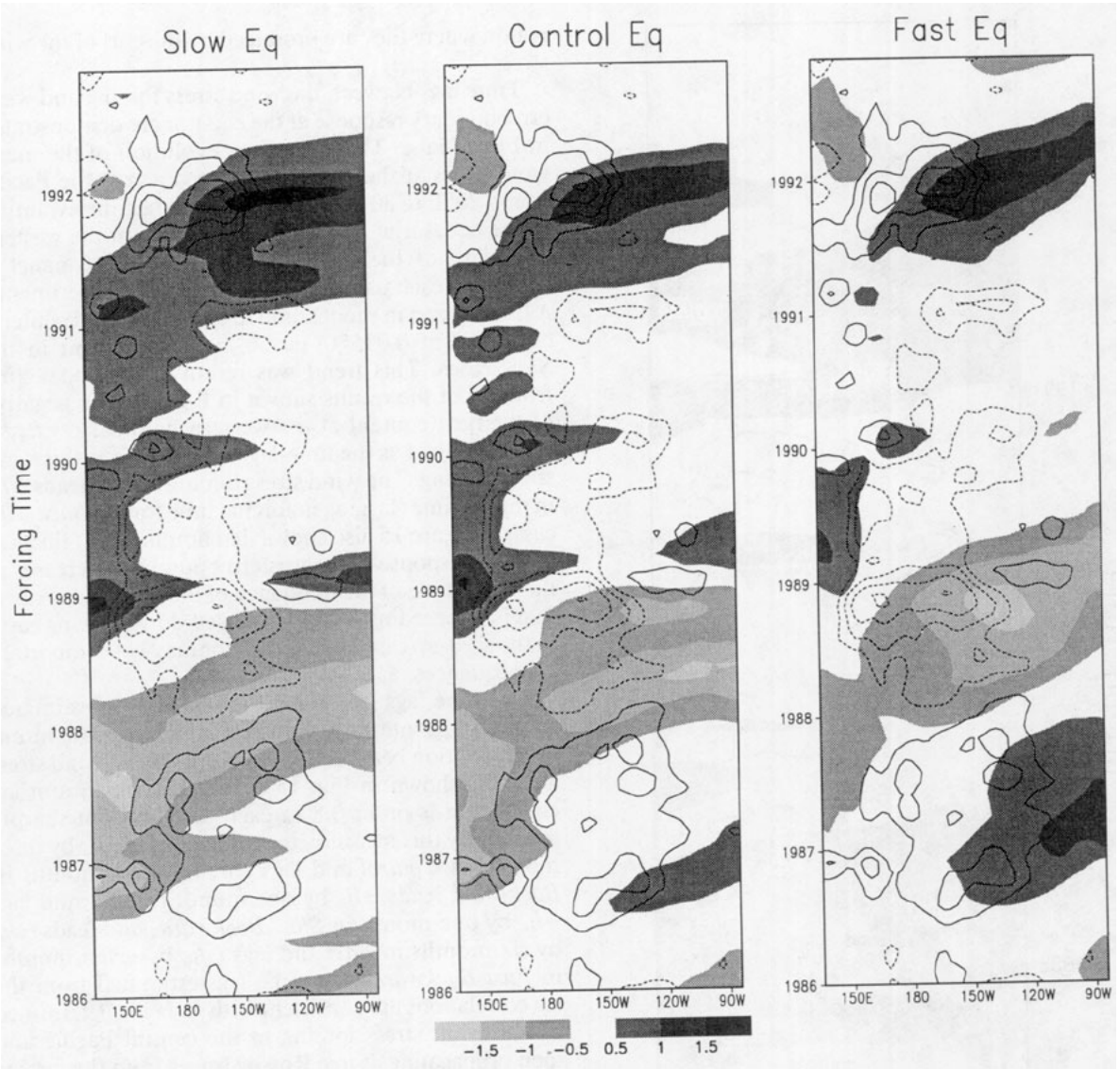

FIG. 13. Time series of equatorial heat content anomalies (°C, shaded) as obtained in the *Slow* experiment, in which the wind stress evolution was slowed down by a factor of 2 (left), *Control* (center), and the *Fast* experiment, in which the forcing was speeded up by a factor of 3 (right). The superimposed contours in each panel are the equatorial wind stress anomalies, contour interval 0.1 dyne, zero contour suppressed (cf. Fig. 4b).

with the wind stress for El Niño timescales. This results from the approximate balance in the zonal momentum equation at the equator

$$0 = -g\frac{\partial h}{\partial x} + \frac{\tau_x}{\rho H}, \qquad (2)$$

where interpretation of h as the thermocline displacement anomaly is now used and x is the distance from the western boundary. Equation (2) holds for timescales long compared to the time it takes a Kelvin wave to cross the basin (Cane 1992).

The predictions of (1) and (2) for the equatorial heat content forced by the observed τ_x were evaluated by integrating (2) from the western boundary, using (1) for the value at the western boundary. Results for *Control* and *Backward* are shown in Fig. 16. The wind stress was multiplied by 80°C (N m^2)$^{-1}$ in order to interpret h as a heat content (cf. Fig. 15). The time lags in (1) were taken from the lag correlations to be $s = 3$ months for *Control,* and $s = -3$ months for *Backward.* The other parameter necessary to obtain the results in Fig. 16 was taken to be $A/x_E = 1/2$, where x_E is the distance from the western to the eastern boundary. The reason for this choice is discussed below. The only difference between the two panels of Fig. 16 is that a lag of 3 months was used to simulate the results from *Control,* and a lead of 3 months was used to simulate the results from *Backward.* The time-delay system is able to capture the very

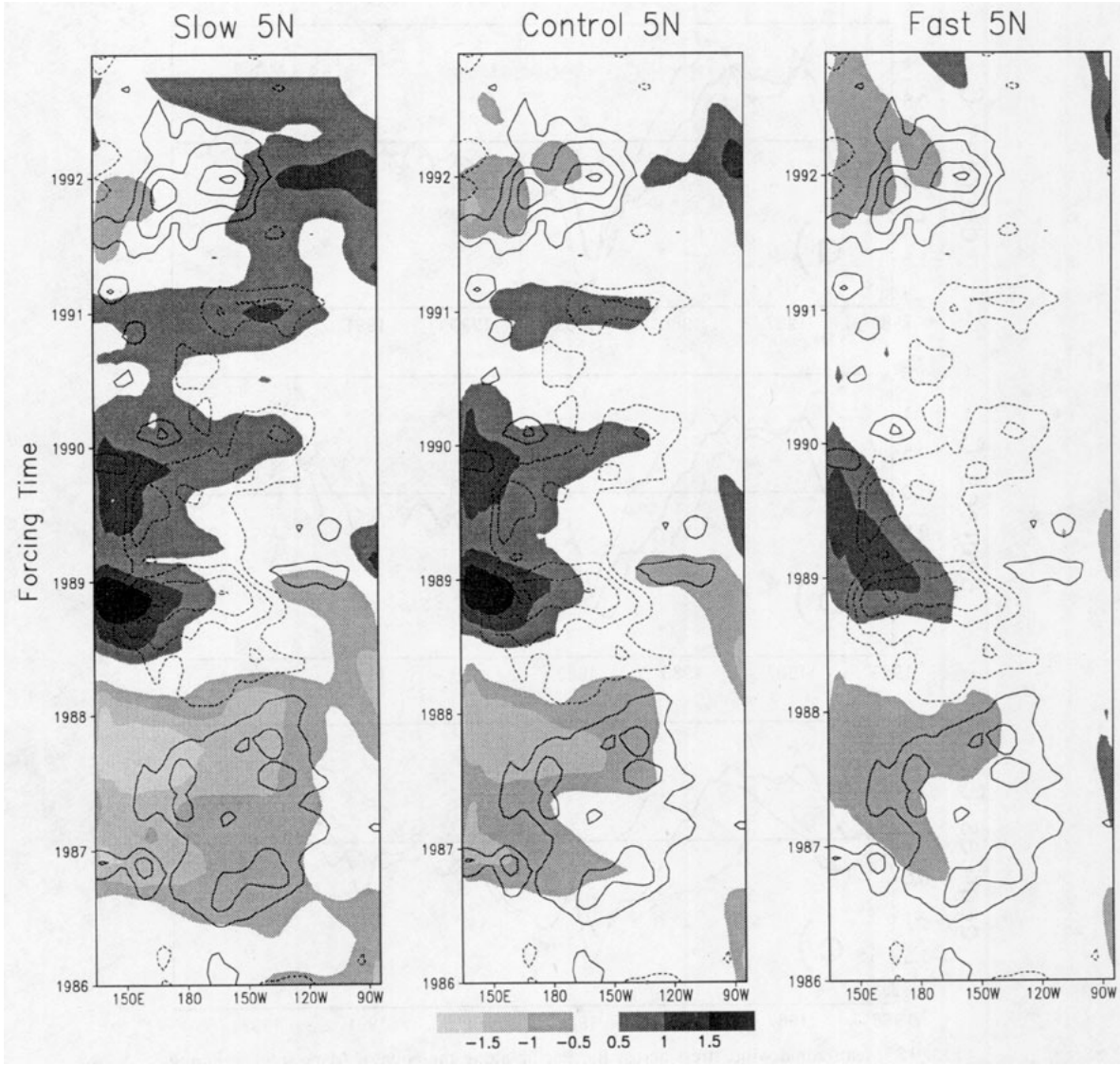

FIG. 14. Time series of heat content anomalies at 5°N (°C, shaded) as obtained in the *Slow* experiment, in which the wind stress evolution was slowed down by a factor of 2 (left), *Control* (center), and the *Fast* experiment, in which the forcing was speeded up by a factor of 3 (right). The superimposed contours in each panel are the equatorial wind stress anomalies, contour interval 0.1 dyn, zero contour suppressed (cf. Fig. 4b).

different appearing heat content evolutions in the two cases, including the slow eastward in model time propagation and the evolution of the zonal mean heat content. The difference between *Control* and *Backward* heat contents (and therefore SST as discussed above) are essentially due to the three-month time delay in the response of the heat content at the western boundary to the wind stress forcing near the dateline.

Equations (1)–(2) also capture many of the characteristics of the results from the *Slow* and *Fast* forward and backward cases, when the frequency dependence of A is taken into account [(8), below]. The predictions for the *Fast* cases begin to differ in the eastern Pacific because the Kelvin wave basin crossing time is comparable to the timescale of the forcing and (2) begins to become inaccurate when the forcing is sped up by a factor of 3.

For the purpose of further discussion, the zonal wind stress will be take to be x independent. The generalization of the results discussed below to more complex structures for τ_x is formally straightforward. Integrating (2) from the western boundary to x and using (1), the relationship

$$h = \frac{1}{\rho g H}\left[-A\overline{\tau_x}(t-s) + x\overline{\tau_x}(t)\right] \qquad (3)$$

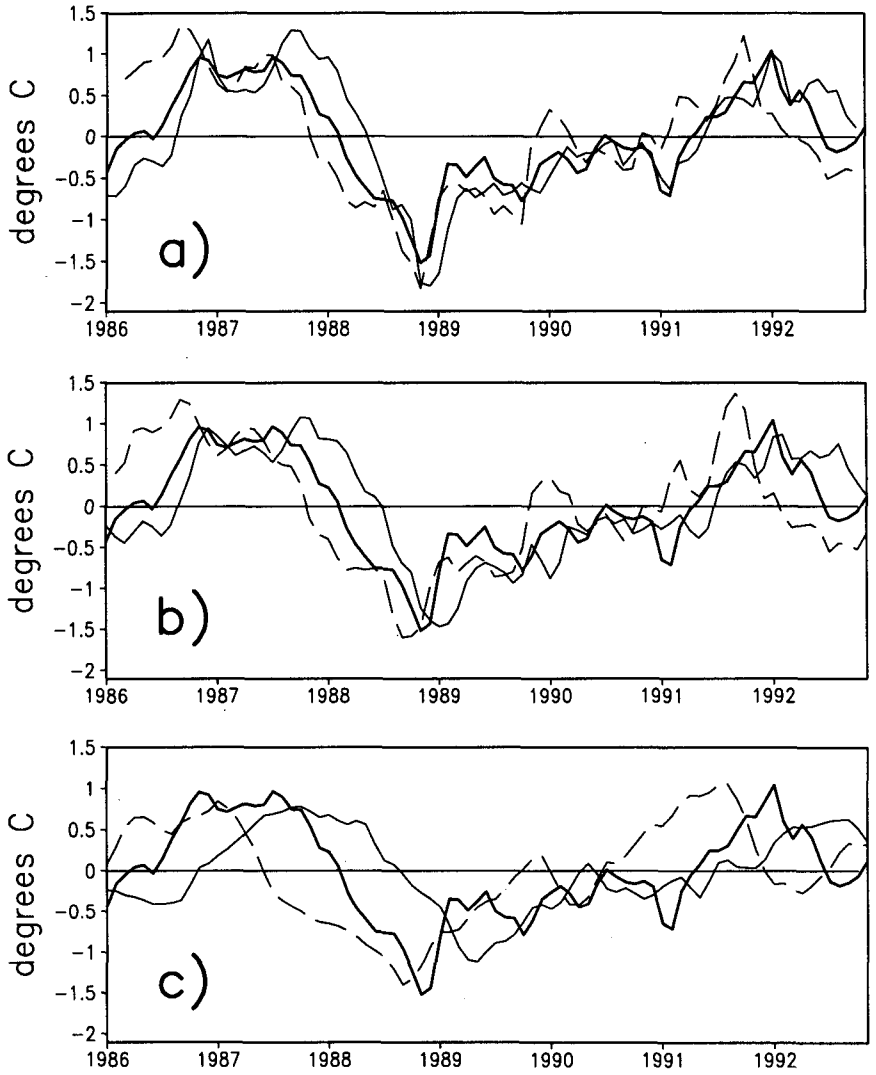

FIG. 15. Mean zonal wind stress across the Pacific along the equator (dark solid line) and negative of the heat content at the equatorial western boundary for wind stress applied forward (light solid line) and backward in model time (light dashed line). (a) *Slow* and *Slow Backward,* in which rate of evolution of wind stress was slowed by a factor of 2, b) *Control* and *Backward,* c) *Fast* and *Fast Backward,* in which evolution was speeded up by a factor of 3. Time axis is forcing time. Wind stress is three month running mean scaled by 80°C $(\text{N m}^2)^{-1}$.

is obtained. Equation (3) is from the familiar class of single Rossby mode time-delay relationships for the thermocline displacements at the equator [e.g., Battisti and Hirst 1989, their Eq. (2.4)].

The response of the mean height at the equator to the wind stress is then found from (3) to be the height evaluated at the midpoint of the basin, $\bar{h} = h(x_E/2)$. Substituting a periodic wind stress forcing with frequency ω into (3),

$$\overline{\tau_x}(t) = Fe^{i\omega t}, \tag{4}$$

and writing the result for the mean height in polar notation $h = |r|e^{i(\omega t+\phi)}$ gives the result that the phase lead ϕ of $h(x)$ is given by

$$\phi = \arctan \frac{\sin(\omega s)}{A^{-1}x - \cos(\omega s)} + \pi, \tag{5}$$

which decreases for $\pi/2 > \omega s > 0$ from $\phi = \pi - \omega s$ at the western boundary to $\phi \approx 0$ where $x/A \gg 1$. The phase of the thermocline depth at the western boundary relative to the forcing is determined by the delay time and forcing frequency, but the phase at other locations is modified by the effect of the wind stress–thermocline slope equilibrium [Eq. (2)].

Equation (5) leads to eastward propagation along the equator when $\omega s < \pi/2$. Slow eastward propagation will occur for values of x where the magnitude of the numerator on the right-hand side of (5) is not much

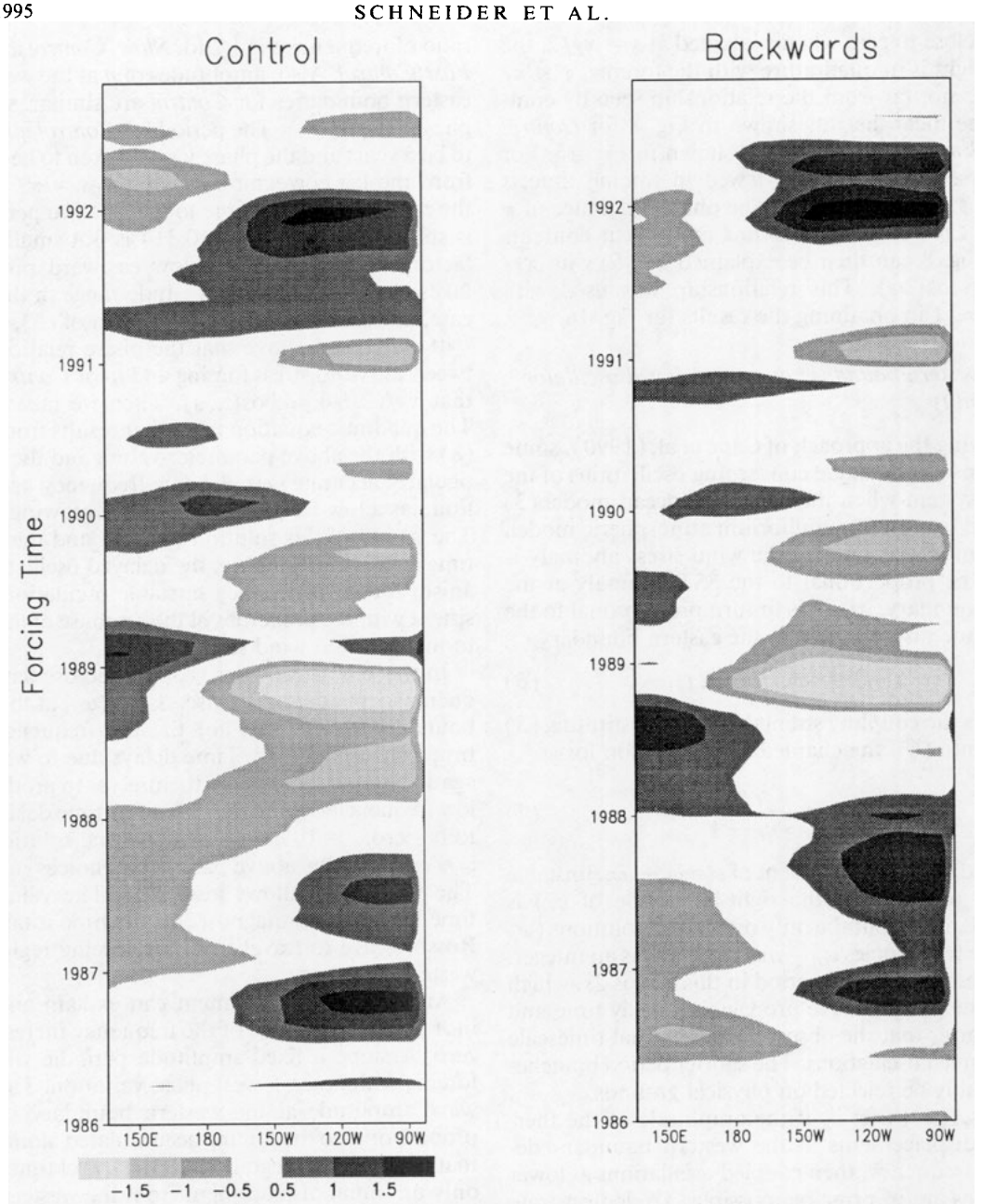

FIG. 16. Equatorial heat content anomalies (°C) from the time delay system, Eqs. (1) and (2), using the observed zonal wind stress anomalies. A time lag of 3 months, corresponding to the *Control* case, is used in the left hand panel. A time lead of 3 months, corresponding to the *Backward* case, is used in the right hand panel.

smaller than the denominator. Rapid eastward phase propagation will occur in regions for which $x/A \gg 1$, particularly near the eastern boundary. In the OGCM the eastward propagation of heat content anomalies in *Control* appears to become significantly faster as the eastern boundary is approached, indicating x_E/A is probably somewhat larger that one in the observed case. For $\omega s \ll 1$ the slowly propagating region will be restricted to a narrow longitude band near $x/A = 1$. The $\omega s \ll 1$ case will approach a nonpropagating equilibrium with the wind stress, corresponding to the fast wave limit. The slow eastward propagation over a substantial longitude band requires that ωs not be too small and is a consequence of the low frequency of the forcing relative to the Kelvin wave timescale and the transmission of information from the forcing region to the western boundary by Rossby waves.

The amplitude $|r| = [A^2 - 2Ax\cos(\omega s) + x^2]^{1/2}$ has a minimum at $x/A = \cos(\omega s)$ for $-\pi/2 < \omega s < \pi/2$. When the denominator of the right-hand side

of (5) is close to zero when evaluated at $x = x_E/2$, the mean height is in quadrature with the forcing, $\phi = \pi/2$. This is not far from the relationship seen by comparing the mean heights shown in Fig. 8 for *Control* and *Backward* and the forcing shown in Fig. 15. For the reversed forcing cases viewed in forcing time, $s < 0$ and $\phi - \pi$ change sign. The phase difference of π between *Control* and *Backward* mean heat contents seen in Fig. 8 can then be explained by (5) with $x_E/(2A) \approx \cos(\omega s)$. This relationship was used with $\cos(\omega s) \approx 1$ in obtaining the results for Fig. 16.

b. *The western boundary and the delayed oscillator instability*

Following the approach of Cane et al. (1990), some deductions can be made concerning oscillations of the coupled system when the simplified ocean model (3) is coupled to a simple equilibrium atmospheric model. In the atmospheric model the wind stress anomaly is taken to be proportional to the SST anomaly at the eastern boundary, which is in turn proportional to the thermocline displacement at the eastern boundary:

$$\overline{\tau_x}(t) = \gamma \rho g H h(x_E, t), \tag{6}$$

where γ is the coupling strength. After substituting (3) and (4) into (6), the characteristic equation for ω

$$e^{i\omega s} = \frac{\gamma A}{\gamma x_E - 1} \tag{7}$$

is obtained. If A is independent of $\omega = \omega_r + i\omega_i$, unstable solutions occur when the right-hand side of (7) is greater than one, but the only oscillatory solutions ($\omega_R \neq 0$) have frequencies $\omega_R = n\pi/s$ where n is an integer. The longest noninfinite period in this case is $2s$, which is twice the Rossby wave propagation delay time and much shorter that the observed interannual timescale of the coupled oscillations. The shorter period branches can probably be rejected on physical grounds.

If $A = A(\omega)$, that is, if the amplitude of the thermocline displacements at the western boundary depends on frequency, then coupled oscillations at lower frequencies are in principle possible. To demonstrate this point and to show that the delayed oscillator mechanism for coupled instability is consistent with the ocean model response to the observed wind stress forcing, (7) is solved for ω using parameter values inferred from the OGCM.

The value for A was estimated by a linear regression of the root-mean-squared amplitudes of the heat content anomalies at the western boundary from *Fast, Control,* and *Slow,* giving

$$A = A_C\left(1.13 - 0.13\,\frac{\omega s}{\omega_C s}\right), \tag{8}$$

where ω represents the frequency of the forcing and the subscript C denotes values taken from *Control.* The ratio of frequencies is 1:2 for *Slow*:*Control* and 3:1 for *Fast*:*Control.* Also, amplitudes of h at the western and eastern boundaries for *Control* are similar, which implies that $\gamma A_C = 1$. The period for *Control* is estimated to be 5 years and the phase lag s is taken to be 3 months from the lag correlations, giving $\omega_C s = \pi/10$. While the ratio of the delay time to the El Niño period, 1:20, is small, the value $\omega_C s = 0.314$ is not small due to a factor of 2π. Therefore, slow eastward propagation takes place over a wide longitude range in the *Control* case, as mentioned in the discussion of (5).

It was noted above that the phase relationship between the wind stress forcing and $\bar{h}$ for *Control* implies that $x_E/(2A_C) \approx \cos(\omega_C s)$. Then we take $\gamma x_E = 2$. The quadratic equation in ωs that results from (7) and (8) with the above parameter values and the (not particularly accurate) $\omega s \ll 1$ low-frequency approximation has a low-frequency oscillatory growing solution. The period of this solution is 4.5 yr and the e-folding time is 2.5 yr. Therefore, the delayed oscillator mechanism for low-frequency unstable oscillations is consistent with the properties of the response of the OGCM to the observed wind stress.

In this empirically derived delayed oscillator, a frequency-dependent response, $A = A(\omega)$, at the western boundary is necessary for the low-frequency ENSO timescale oscillations. Time delays due to wave propagation are not enough by themselves to produce these low frequencies. Similarly, when the time delay is taken to be zero, $s = 0$, in (7), only neutral solutions (with $\omega = \omega_C$ using the above parameter choices) are found. The time delay allows instability. The value for the time lag has been diagnosed as the time it takes a free Rossby wave to travel from the forcing region to the western boundary.

An interference argument can explain an increase in A as the magnitude of the frequency increases from zero. Assume a fixed-amplitude periodic wind stress forcing with no east–west phase variation. The Rossby wave amplitude at the western boundary should be proportional to the forcing accumulated along its path, that is, the time integral. Since the travel time depends only on initial displacement from the western boundary, the western boundary amplitude will be proportional to the mean forcing along the path. As the frequency of the forcing increases, a Rossby wave ray path originating from strong forcing in the central Pacific will tend to encounter reduced forcing, or even forcing of opposite sign, relative to what it would encounter with lower-frequency forcing, leading to a decrease in amplitude at the western boundary as forcing frequency increases.

The analytic solution for $h(x = x_E)$, the equatorial eastern boundary thermocline displacement in response to periodic x-independent wind stress forcing for a linear shallow water ocean model [Cane and Sarachik 1981; Cane et al. 1990, their Eq. (11)], gives $h(x = x_E) \propto (i\omega)^{1/2}$ as $\omega \to 0$. The western boundary

response can be found using (2). If the basin is wide enough, the magnitude of the response at the western boundary will decrease as ω increases, in agreement with the OGCM results shown in Fig. 15 and the interference argument.

5. Summary

A number of experiments were performed forcing an ocean general circulation model of the tropical Pacific with the observed wind stress for 1986–1992. These experiments were designed to help understand the processes that contribute to the slow timescale and oscillatory nature of El Niño.

A control case produced a realistic simulation of the observed evolution of near equatorial SST and heat content anomalies. Another case applied the same wind stress forcing as the control case, except backward in time. Comparison of the forward and reversed forcing cases showed that the SST was in equilibrium with the wind stress forcing in the central Pacific. In the eastern Pacific the SST departed from equilibrium with the wind stress forcing due to sensitivity to thermocline displacements. No evidence was found for a significant departure from equilibrium due to heat storage in the mixed layer. The heat content at the equator exhibited slow eastward propagation in both the forward and reversed cases and hence was not in equilibrium with the wind stress. It was shown that only the longitudinal mean of the heat content was not in equilibrium with the wind stress; the deviation from this mean heat content was the same for both experiments on El Niño timescales. The heat content close to but off the equator exhibited westward propagation in both cases and therefore was not in equilibrium with the wind stress.

With the aid of additional experiments in which the evolution of the wind stress forcing was slowed down and sped up, it was found that the propagation speed of the off-equatorial westward-moving disturbances was approximately independent of the frequency of the forcing with a value of about 0.5 m s^{-1}. The result was consistent with these disturbances being low-order freely propagating equatorially trapped Rossby waves. These Rossby waves cause the heat content anomalies near the western boundary of the ocean at the equator to be highly negatively correlated with the equatorial wind stress anomalies near the dateline, with a time lag of about three months. This behavior can explain the characteristics of the low-frequency response of the equatorial thermocline displacements at all longitudes, as well as the behavior of the mean value in our numerical experiments.

A simple time-delay equation was shown to empirically fit the numerical results for the response of the equatorial thermocline displacements to the imposed wind stress forcing. This equation has two adjustable parameters, the time delay due to Rossby wave propagation and the amplitude of the time-delayed response at the western boundary. These parameters were estimated from the results of the numerical experiments.

The results from our experiments are consistent with the hypothesis that the slow timescale and oscillatory nature of El Niño are due to the delayed oscillator mechanism. The mean heat content at the equator carries the memory of the system and transmits this memory to the atmosphere through the eastern and central Pacific SST anomalies. Equatorial wind stress anomalies excite westward propagating free Rossby waves. Thermocline displacements with largest amplitudes off the equator travel as Rossby waves to the western boundary. When these displacements reach the western boundary they set the value of the thermocline displacement at the western boundary at the equator. Since the east–west thermocline slope at the equator is in equilibrium with the local wind stress, the thermocline at all longitudes adjusts instantaneously (i.e., at Kelvin wave timescales) to maintain the same slope with the new value of the displacement at the western boundary.

A commonly employed simple coupled model closure, which effectively assumes that the structure of wind stress anomalies was the observed structure used in the numerical experiments, was introduced. The amplitude of this wind stress forcing was taken to be proportional to thermocline displacements at the eastern boundary. The oceanic component of the coupled model was the time-delay equation that gives the thermocline displacements as a function of the wind stress. In the context of this highly simplified model, a finite time lag was shown to be necessary for coupled instability, while a frequency dependence of the amplitude of the western boundary response to the forcing was shown to be necessary for low-frequency coupled oscillations. The parameter dependencies estimated from the numerical experiments to best fit the observed system were shown to be consistent with unstable low-frequency coupled oscillations.

In our interpretation of the results, the mechanism for El Niño is the delayed oscillator as developed by Schopf and Suarez (1988), Battisti and Hirst (1989), Schopf and Suarez (1990), and Cane et al. (1990). Our numerical results and interpretation are in general agreement with those found by Chao and Philander's (1993); however, in contrast to the Chao and Philander (1993), we identify freely propagating equatorial Rossby waves in the western Pacific and assign an important role to these free waves.

In terms of the limiting cases discussed by Jin and Neelin (1993a), Neelin and Jin (1993), and Jin and Neelin (1993b), we find that the coupled system is best described as slow wave–fast SST. That is the ocean is far from equilibrium with the wind stress forcing, and the heat storage in the mixed layer is unimportant in the heat budget of the surface layer of the ocean. Our simplified coupled model for this regime gives the result that the time delay is necessary for coupled instability,

and frequency dependence of the Rossby wave amplitudes at the western boundary is necessary for the long period of the coupled oscillations. This frequency dependence is present in the model of Cane et al. (1990) but not in that of Battisti and Hirst (1989) or the single Rossby wave reflection case of Schopf and Suarez (1990).

Since the SST and heat content anomalies of the control integration are in some ways close to the observed, it is legitimate to suppose that model properties implied in this experiment are also properties of the real tropical Pacific Ocean. These properties are as follows.

- SST anomalies in the equatorial western Pacific are in near-equilibrium with the wind stress.
- SST anomalies are strongly influenced by heat content anomalies in the eastern equatorial Pacific.
- Equatorial heat content anomalies with the zonal mean removed are approximately in equilibrium with the observed wind stress forcing anomalies. This condition determines the slope of the equatorial thermocline.
- Zonal mean equatorial heat content anomalies are not in equilibrium with the observed wind stress forcing anomalies.
- The westward propagating off-equatorial heat content anomalies in the western Pacific are freely propagating Rossby waves excited by wind stress forcing near the date line.
- These Rossby waves determine the value of the equatorial heat content anomalies at the western boundary when they arrive there, which is sufficient to determine the equatorial heat content at all longitudes given the thermocline slope.

Acknowledgments. This research was supported by NOAA Grant NA26-GP0149 and NSF Grants ATM-9341271 and ATM-9342469. We thank Drs. Ji and Leetmaa of the National Meteorological Center for supplying us with the results from their preliminary retrospective analysis of the tropical Pacific Ocean. We thank Drs. Zebiak, Cane, McPhaden, Latif, Philander, Neelin, Sarachik, Schopf, Suarez, and Battisti for their comments and suggestions, many of which have been incorporated into the paper.

REFERENCES

Barnett, T. P., M. Latif, N. Graham, M. Flügel, S. Pazan, and W. White, 1993: ENSO and ENSO-related predictability. Part I: Prediction of equatorial Pacific sea surface temperature with a hybrid coupled ocean–atmosphere model. *J. Climate,* **6,** 1545–1566.

Battisti, D. S., and A. C. Hirst, 1989: Interannual variability in a tropical atmosphere–ocean model: Influence of the basic state, ocean geometry, and nonlinearity. *J. Atmos. Sci.,* **46,** 1687–1712.

Bjerknes, J., 1966: A possible response of the atmospheric Hadley circulation to equatorial anomalies of ocean temperature. *Tellus,* **18,** 820–828.

——, 1969: Atmospheric teleconnections from the equatorial Pacific. *Mon. Wea. Rev.,* **97,** 163–172.

Bryan, K., and L. Lewis, 1979: A water mass model of the world ocean. *J. Geophys. Res.,* **84,** 2503–2517.

Cane, M. A., 1992: Comments on "The fast-wave limit and interannual oscillations." *J. Atmos. Sci.,* **49,** 1947–1949.

——, and E. S. Sarachik, 1981: The response of a linear baroclinic equatorial ocean to periodic forcing. *J. Mar. Res.,* **39,** 651–693.

——, and S. E. Zebiak, 1987: Prediction of El Niño events using a physical model. *Atmospheric and Oceanic Variability,* H. Cattel, Ed., Roy. Meteor. Soc., 153–182.

——, M. Münnich, and S. E. Zebiak, 1990: A study of self-excited oscillations of the tropical ocean–atmosphere system. Part I: Linear analysis. *J. Atmos. Sci.,* **47,** 1562–1577.

Chao, Y., and S. G. H. Philander, 1993: On the structure of the Southern Oscillation. *J. Climate,* **6,** 450–469.

Hao, Z., J. D. Neelin, and F.-F. Jin, 1993: Nonlinear tropical air–sea interaction in the fast-wave limit. *J. Climate,* **6,** 1523–1544.

Huang, B., and E. K. Schneider, 1995: The response of an ocean general circulation model to surface wind stress produced by an atmospheric general circulation model. *Mon. Wea. Rev.,* **123,** 3059–3085.

——, J. A. Carton, and J. Shukla, 1994: A numerical simulation of the variability in the tropical Atlantic Ocean, 1980–88. *J. Phys. Oceanogr.,* **24,** 835–854.

Jin, F.-F., and J. D. Neelin, 1993a: Modes of interannual tropical ocean–atmosphere interaction—a unified view. Part I: Numerical results. *J. Atmos. Sci.,* **50,** 3477–3503.

——, and ——, 1993b: Modes of interannual tropical ocean–atmosphere interaction—a unified view. Part III: Analytical results in fully coupled cases. *J. Atmos. Sci.,* **50,** 3523–3540.

Latif, M., A. Sterl, E. Maier-Reimer, and M. M. Junge, 1993: Climate variability in a coupled GCM. Part I: The tropical Pacific. *J. Climate,* **6,** 5–21.

Lau, N.-C., S. G. H. Philander, and M. J. Nath, 1992: Simulation of ENSO-like phenomena with a low resolution coupled GCM of the global ocean and atmosphere. *J. Climate,* **5,** 284–307.

Leetmaa, A., and M. Ji, 1989: Operational hindcasting of the tropical Pacific. *Dyn. Atmos. Oceans,* **13,** 465–490.

Levitus, S., 1982: *Climatological Atlas of the World Ocean.* NOAA Prof. Paper No. 13, U.S. Dept. of Commerce, 173 pp.

McPhaden, M. J., and B. A. Taft, 1988: Dynamics of seasonal and intraseasonal variability in the eastern equatorial Pacific. *J. Phys. Oceanogr.,* **18,** 1713–1732.

Miller, A. J., T. P. Barnett, and N. E. Graham, 1993: A comparison of some tropical ocean models: Hindcast skill and El Niño evolution. *J. Phys. Oceanogr.,* **23,** 1567–1591.

Neelin, J. D., 1990: A hybrid coupled general circulation model for El Niño studies. *J. Atmos. Sci.,* **47,** 674–693.

——, 1991: The slow sea surface temperature mode and the fast-wave limit: Analytic theory for tropical interannual oscillations and experiments in a hybrid coupled model. *J. Atmos. Sci.,* **48,** 584–606.

——, and F.-F. Jin, 1993: Modes of interannual tropical ocean–atmosphere interaction—a unified view. Part II: Analytical results in the weak-coupling limit. *J. Atmos. Sci.,* **50,** 3504–3522.

——, Z. Hao, and F.-F. Jin, 1992a: Reply. *J. Atmos. Sci.,* **49,** 1950–1953.

——, and Coauthors, 1992b: Tropical air–sea interaction in general circulation models. *Climate Dyn.,* **7,** 73–104.

——, M. Latif, and F.-F. Jin, 1994: Dynamics of coupled ocean–atmosphere models: The tropical problem. *Ann. Rev. Fluid Mech.,* **26,** 617–659.

Oberhuber, J. M., 1988: *An atlas based on the 'COADS' data set: The budgets of heat, buoyancy and turbulent kinetic energy at the surface of the global ocean.* Report 15, Max-Planck-Institut für Meteorologie, Hamburg, 199 pp.

Oort, A. H., 1983: Global atmospheric circulation statistics, 1958–1973. NOAA Prof. Paper No. 14, U.S. Govt. Printing Office, Washington, D.C., 180 pp. + 47 microfiches.

Pacanowski, R., and S. G. H. Philander, 1981: Parameterization of vertical mixing in numerical models of tropical oceans. *J. Phys. Oceanogr.*, **11,** 1443–1451.

Philander, S. G. H., 1979: Variability of the tropical ocean. *Dyn. Atmos. Oceans,* **3,** 191–208.

——, 1981: The response of equatorial oceans to a relaxation of the trade winds. *J. Phys. Oceanogr.*, **11,** 176–189.

——, 1985: El Niño and La Niña. *J. Atmos. Sci.*, **42,** 2652–2662.

——, and R. C. Pacanowski, 1986: A model of the seasonal cycle in the tropical Atlantic Ocean. *J. Geophys. Res.*, **91,** 14 192–14 206.

——, and W. J. Hurlin, 1988: The heat budget of the tropical Pacific Ocean in a simulation of the 1983–83 El Niño. *J. Phys. Oceanogr.*, **18,** 926–931.

——, T. Yamagata, and R. C. Pacanowski, 1984: Unstable air–sea interactions in the Tropics. *J. Atmos. Sci.*, **41,** 604–613.

Robertson, A. W., C.-C. Ma, C. R. Mechoso, and M. Ghil, 1995: Simulation of the tropical Pacific climate with a coupled ocean–atmosphere general circulation model. Part II: Interannual variability. *J. Climate,* **8,** 1199–1216.

Rosati, A., and K. Miyakoda, 1988: A general circulation model for upper ocean simulation. *J. Phys. Oceanogr.*, **18,** 1601–1626.

Schopf, P. S., and M. J. Suarez, 1988: Vacillations in a coupled ocean–atmosphere model. *J. Atmos. Sci.*, **45,** 549–566.

——, and ——, 1990: Ocean wave dynamics and the timescale of ENSO. *J. Phys. Oceanogr.*, **20,** 629–645.

Suarez, M. J., and P. S. Schopf, 1988: A delayed action oscillator for ENSO. *J. Atmos. Sci.*, **45,** 3283–3287.

Trenberth, K. E., W. G. Large, and J. G. Olson, 1990: The mean annual cycle in global ocean wind stress. *J. Phys. Oceanogr.*, **20,** 1742–1760.

Wyrtki, K., 1985: Water displacements in the Pacific and the genesis of El Niño cycles. *J. Geophys. Res.*, **90,** 7129–7132.

Zebiak, S. E., 1989: Oceanic heat content variability and El Niño cycles. *J. Phys. Oceanogr.*, **19,** 475–486.

——, and M. A. Cane, 1987: A model El Niño Southern Oscillation. *Mon. Wea. Rev.*, **115,** 2262–2278.